Dissociation of virtual photons in events with a leading proton at HERA

ZEUS Collaboration

Abstract

The ZEUS detector has been used to study dissociation of virtual photons in events with a leading proton, $\gamma^*p \to Xp$, in e^+p collisions at HERA. The data cover photon virtualities in two ranges, $0.03 < Q^2 < 0.60 \text{ GeV}^2$ and $2 < Q^2 < 100 \text{ GeV}^2$, with $M_X > 1.5 \text{ GeV}$, where M_X is the mass of the hadronic final state, X. Events were required to have a leading proton, detected in the ZEUS leading proton spectrometer, carrying at least 90% of the incoming proton energy. The cross section is presented as a function of t, the squared four-momentum transfer at the proton vertex, Φ , the azimuthal angle between the positron scattering plane and the proton scattering plane, and Q^2 . The data are presented in terms of the diffractive structure function, $F_2^{D(3)}$. A next-to-leading-order QCD fit to the higher- Q^2 data set and to previously published diffractive charm production data is presented.

The ZEUS Collaboration

S. Chekanov, M. Derrick, J.H. Loizides¹, S. Magill, S. Miglioranzi¹, B. Musgrave, J. Repond, R. Yoshida

Argonne National Laboratory, Argonne, Illinois 60439-4815, USA ⁿ

M.C.K. Mattingly

Andrews University, Berrien Springs, Michigan 49104-0380, USA

N. Pavel

Institut für Physik der Humboldt-Universität zu Berlin, Berlin, Germany

- P. Antonioli, G. Bari, M. Basile, L. Bellagamba, D. Boscherini, A. Bruni, G. Bruni,
- G. Cara Romeo, L. Cifarelli, F. Cindolo, A. Contin, M. Corradi, S. De Pasquale, P. Giusti,
- G. Iacobucci, A. Margotti, T. Massam, A. Montanari, R. Nania, F. Palmonari, A. Pesci,
- A. Polini, L. Rinaldi, G. Sartorelli, A. Zichichi University and INFN Bologna, Bologna, Italy ^e
- G. Aghuzumtsyan, D. Bartsch, I. Brock, S. Goers, H. Hartmann, E. Hilger, P. Irrgang, H.-
- P. Jakob, O. Kind, U. Meyer, E. Paul², J. Rautenberg, R. Renner, J. Tandler³, K.C. Voss, M. Wang

Physikalisches Institut der Universität Bonn, Bonn, Germany ^b

- D.S. Bailey⁴, N.H. Brook, J.E. Cole, G.P. Heath, T. Namsoo, S. Robins, M. Wing H.H. Wills Physics Laboratory, University of Bristol, Bristol, United Kingdom ^m
- M. Capua, L. Iannotti⁵, A. Mastroberardino, M. Schioppa, G. Susinno Calabria University, Physics Department and INFN, Cosenza, Italy ^e
- J.Y. Kim, I.T. Lim, K.J. Ma, M.Y. Pac⁶

Chonnam National University, Kwangju, South Korea ^g

M. Helbich, Y. Ning, Z. Ren, W.B. Schmidke, F. Sciulli

 $Nevis\ Laboratories,\ Columbia\ University,\ Irvington\ on\ Hudson,\ New\ York\ 10027\ ^o$

- J. Chwastowski, A. Eskreys, J. Figiel, A. Galas, K. Olkiewicz, P. Stopa, L. Zawiejski Institute of Nuclear Physics, Cracow, Poland i
- L. Adamczyk, T. Bołd, I. Grabowska-Bołd⁷, D. Kisielewska, A.M. Kowal, J. Łukasik, M. Przybycień, L. Suszycki, D. Szuba, J. Szuba⁸

Faculty of Physics and Nuclear Techniques, AGH-University of Science and Technology, Cracow, Poland ^p

A. Kotański⁹, W. Słomiński

Department of Physics, Jagellonian University, Cracow, Poland

- V. Adler, U. Behrens, I. Bloch, K. Borras, D. Dannheim¹⁰, G. Drews, J. Fourletova,
- U. Fricke, A. Geiser, D. Gladkov, P. Göttlicher¹¹, O. Gutsche, T. Haas, W. Hain, C. Horn,
- B. Kahle, U. Kötz, H. Kowalski, G. Kramberger, H. Labes, D. Lelas¹², H. Lim, B. Löhr,
- R. Mankel, I.-A. Melzer-Pellmann, C.N. Nguyen, D. Notz, A.E. Nuncio-Quiroz, A. Raval,
- U. Schneekloth, A. Stifutkin, U. Stösslein, G. Wolf, C. Youngman, W. Zeuner Deutsches Elektronen-Synchrotron DESY, Hamburg, Germany

S. Schlenstedt

Deutsches Elektronen-Synchrotron DESY, Zeuthen, Germany

G. Barbagli, E. Gallo, C. Genta, P. G. Pelfer University and INFN, Florence, Italy ^e

A. Bamberger, A. Benen, F. Karstens, D. Dobur, N.N. Vlasov¹³
Fakultät für Physik der Universität Freiburg i.Br., Freiburg i.Br., Germany ^b

P.J. Bussey, A.T. Doyle, J. Ferrando, J. Hamilton, S. Hanlon, D.H. Saxon, I.O. Skillicorn Department of Physics and Astronomy, University of Glasgow, Glasgow, United Kingdom ^m

I. Gialas¹⁴

Department of Engineering in Management and Finance, Univ. of Aegean, Greece

- T. Carli, T. Gosau, U. Holm, N. Krumnack, E. Lohrmann, M. Milite, H. Salehi, P. Schleper,
- T. Schörner-Sadenius, S. Stonjek¹⁵, K. Wichmann, K. Wick, A. Ziegler, Ar. Ziegler *Hamburg University, Institute of Exp. Physics, Hamburg, Germany* ^b
- C. Collins-Tooth¹⁶, C. Foudas, R. Gonçalo¹⁷, K.R. Long, A.D. Tapper Imperial College London, High Energy Nuclear Physics Group, London, United Kingdom ^m

P. Cloth, D. Filges

Forschungszentrum Jülich, Institut für Kernphysik, Jülich, Germany

M. Kataoka¹⁸, K. Nagano, K. Tokushuku¹⁹, S. Yamada, Y. Yamazaki *Institute of Particle and Nuclear Studies, KEK, Tsukuba, Japan* ^f

A.N. Barakbaev, E.G. Boos, N.S. Pokrovskiy, B.O. Zhautykov

Institute of Physics and Technology of Ministry of Education and Science of Kazakhstan, Almaty, Kazakhstan

D. Son

Kyungpook National University, Center for High Energy Physics, Daegu, South Korea ⁹

J. de Favereau, K. Piotrzkowski

Institut de Physique Nucléaire, Université Catholique de Louvain, Louvain-la-Neuve, Belgium

F. Barreiro, C. Glasman²⁰, O. González, L. Labarga, J. del Peso, E. Tassi, J. Terrón, M. Zambrana

Departamento de Física Teórica, Universidad Autónoma de Madrid, Madrid, Spain l

M. Barbi, F. Corriveau, C. Liu, S. Padhi, M. Plamondon, D.G. Stairs, R. Walsh, C. Zhou Department of Physics, McGill University, Montréal, Québec, Canada H3A 2T8 ^a

T. Tsurugai

Meiji Gakuin University, Faculty of General Education, Yokohama, Japan ^f

A. Antonov, P. Danilov, B.A. Dolgoshein, V. Sosnovtsev, S. Suchkov *Moscow Engineering Physics Institute, Moscow, Russia* ^j

R.K. Dementiev, P.F. Ermolov, I.I. Katkov, L.A. Khein, I.A. Korzhavina, V.A. Kuzmin, B.B. Levchenko, O.Yu. Lukina, A.S. Proskuryakov, L.M. Shcheglova, S.A. Zotkin $Moscow\ State\ University,\ Institute\ of\ Nuclear\ Physics,\ Moscow,\ Russia^k$

I. Abt, C. Büttner, A. Caldwell, X. Liu, J. Sutiak Max-Planck-Institut für Physik, München, Germany

N. Coppola, G. Grigorescu, S. Grijpink, A. Keramidas, E. Koffeman, P. Kooijman, E. Maddox, A. Pellegrino, S. Schagen, H. Tiecke, M. Vázquez, L. Wiggers, E. de Wolf *NIKHEF and University of Amsterdam, Amsterdam, Netherlands* ^h

N. Brümmer, B. Bylsma, L.S. Durkin, T.Y. Ling *Physics Department, Ohio State University, Columbus, Ohio* 43210 ⁿ

P.D. Allfrey, M.A. Bell, A.M. Cooper-Sarkar, A. Cottrell, R.C.E. Devenish, B. Foster, G. Grzelak, C. Gwenlan²¹, T. Kohno, S. Patel, P.B. Straub, R. Walczak Department of Physics, University of Oxford, Oxford United Kingdom ^m

P. Bellan, A. Bertolin, R. Brugnera, R. Carlin, R. Ciesielski, F. Dal Corso, S. Dusini, A. Garfagnini, S. Limentani, A. Longhin, A. Parenti, M. Posocco, L. Stanco, M. Turcato Dipartimento di Fisica dell' Università and INFN, Padova, Italy ^e

E.A. Heaphy, F. Metlica, B.Y. Oh, J.J. Whitmore 22

Department of Physics, Pennsylvania State University, University Park, Pennsylvania 16802°

Y. Iga

Polytechnic University, Sagamihara, Japan ^f

G. D'Agostini, G. Marini, A. Nigro

Dipartimento di Fisica, Università 'La Sapienza' and INFN, Rome, Italy ^e

J.C. Hart

 $Rutherford\ Appleton\ Laboratory,\ Chilton,\ Didcot,\ Oxon,\ United\ Kingdom\ ^m$

D. Epperson²³, C. Heusch, H. Sadrozinski, A. Seiden, R. Wichmann²⁴, D.C. Williams *University of California, Santa Cruz, California 95064*, USA ⁿ

I.H. $Park^{25}$

Department of Physics, Ewha Womans University, Seoul, Korea

H. Abramowicz, A. Gabareen, S. Kananov, A. Kreisel, A. Levy Raymond and Beverly Sackler Faculty of Exact Sciences, School of Physics, Tel-Aviv University, Tel-Aviv, Israel ^d

M. Kuze

Department of Physics, Tokyo Institute of Technology, Tokyo, Japan ^f

T. Fusayasu, S. Kagawa, T. Tawara, T. Yamashita Department of Physics, University of Tokyo, Tokyo, Japan ^f

R. Hamatsu, T. Hirose², M. Inuzuka, H. Kaji, S. Kitamura²⁶, K. Matsuzawa *Tokyo Metropolitan University, Department of Physics, Tokyo, Japan* ^f

 $N.\ Cartiglia,\ R.\ Cirio,\ M.\ Costa,\ M.I.\ Ferrero,\ S.\ Maselli,\ V.\ Monaco,\ C.\ Peroni,\ M.C.\ Petrucci^{27},$

R. Sacchi, A. Solano, A. Staiano

Università di Torino and INFN, Torino, Italy ^e

M. Arneodo, M. Ruspa

Università del Piemonte Orientale, Novara, and INFN, Torino, Italy e

S. Fourletov, T. Koop, J.F. Martin, A. Mirea Department of Physics, University of Toronto, Toronto, Ontario, Canada M5S 1A7^a

J.M. Butterworth 28 , R. Hall-Wilton, T.W. Jones, M.R. Sutton 4 , C. Targett-Adams Physics and Astronomy Department, University College London, London, United Kingdom m

J. Ciborowski²⁹, P. Łużniak³⁰, R.J. Nowak, J.M. Pawlak, J. Sztuk³¹, T. Tymieniecka, A. Ukleja, J. Ukleja³², A.F. Żarnecki

Warsaw University, Institute of Experimental Physics, Warsaw, Poland

M. Adamus, P. Plucinski

Institute for Nuclear Studies, Warsaw, Poland

Y. Eisenberg, D. Hochman, U. Karshon, M.S. Lightwood, M. Riveline Department of Particle Physics, Weizmann Institute, Rehovot, Israel ^c

A. Everett, L.K. Gladilin³³, D. Kçira, S. Lammers, L. Li, D.D. Reeder, M. Rosin, P. Ryan, A.A. Savin, W.H. Smith

Department of Physics, University of Wisconsin, Madison, Wisconsin 53706, USA ⁿ

S. Dhawan

Department of Physics, Yale University, New Haven, Connecticut 06520-8121, USA n

- S. Bhadra, C.D. Catterall, G. Hartner, S. Menary, U. Noor, M. Soares, J. Standage,
- J. Whyte, C. Ying

 $Department\ of\ Physics,\ York\ University,\ Ontario,\ Canada\ M3J\ 1P3\ ^a$

- ¹ also affiliated with University College London, UK
- ² retired
- 3 self-employed
- ⁴ PPARC Advanced fellow
- ⁵ now at Consoft Sistemi s.r.l., Torino, Italy
- ⁶ now at Dongshin University, Naju, South Korea
- 7 partly supported by Polish Ministry of Scientific Research and Information Technology, grant no. 2P03B 12225
- 8 partly supported by Polish Ministry of Scientific Research and Information Technology, grant no.2P03B 12625
- ⁹ supported by the Polish State Committee for Scientific Research, grant no. 2 P03B 09322
- ¹⁰ now at Columbia University, N.Y., USA
- ¹¹ now at DESY group FEB, Hamburg, Germany
- 12 now at LAL, Université de Paris-Sud, IN2P3-CNRS, Orsay, France
- ¹³ partly supported by Moscow State University, Russia
- 14 also affiliated with DESY
- 15 now at University of Oxford, UK $\,$
- ¹⁶ now at the Department of Physics and Astronomy, University of Glasgow, UK
- 17 now at Royal Holloway University of London, UK
- 18 also at Nara Women's University, Nara, Japan
- ¹⁹ also at University of Tokyo, Japan
- ²⁰ Ramón y Cajal Fellow
- 21 PPARC Postdoctoral Research Fellow
- ²² on leave of absence at The National Science Foundation, Arlington, VA, USA
- 23 now at California Polytechnic State University, San Luis Obisbo, USA
- ²⁴ now at DESY, Hamburg, Germany
- 25 supported by the Intramural Research Grant of Ewha Womans University
- 26 present address: Tokyo Metropolitan University of Health Sciences, Tokyo 116-8551, Japan
- $^{\rm 27}$ now at University of Perugia, Perugia, Italy
- ²⁸ also at University of Hamburg, Alexander von Humboldt Fellow
- 29 also at Łódź University, Poland
- ³⁰ Łódź University, Poland
- 31 Łódź University, Poland, supported by the KBN grant 2P03B12925
- 32 supported by the KBN grant 2P03B12725
- ³³ on leave from Moscow State University, Russia, partly supported by the Weizmann Institute via the U.S.-Israel Binational Science Foundation

- ^a supported by the Natural Sciences and Engineering Research Council of Canada (NSERC)
- b supported by the German Federal Ministry for Education and Research (BMBF), under contract numbers HZ1GUA 2, HZ1GUB 0, HZ1PDA 5, HZ1VFA 5
- supported in part by the MINERVA Gesellschaft für Forschung GmbH, the Israel Science Foundation (grant no. 293/02-11.2), the U.S.-Israel Binational Science Foundation and the Benozyio Center for High Energy Physics
- d supported by the German-Israeli Foundation and the Israel Science Foundation
- ^e supported by the Italian National Institute for Nuclear Physics (INFN)
- supported by the Japanese Ministry of Education, Culture, Sports, Science and Technology (MEXT) and its grants for Scientific Research
- g supported by the Korean Ministry of Education and Korea Science and Engineering Foundation
- h supported by the Netherlands Foundation for Research on Matter (FOM)
- supported by the Polish State Committee for Scientific Research, grant no. 620/E-77/SPB/DESY/P-03/DZ 117/2003-2005
- j partially supported by the German Federal Ministry for Education and Research (BMBF)
- supported by RF President grant N 1685.2003.2 for the leading scientific schools and by the Russian Ministry of Industry, Science and Technology through its grant for Scientific Research on High Energy Physics
- supported by the Spanish Ministry of Education and Science through funds provided by CICYT
- m supported by the Particle Physics and Astronomy Research Council, UK
- ⁿ supported by the US Department of Energy
- o supported by the US National Science Foundation
- p supported by the Polish Ministry of Scientific Research and Information Technology, grant no. 112/E-356/SPUB/DESY/P-03/DZ~116/2003-2005

1 Introduction

In diffractive processes in hadron-hadron or photon-hadron collisions, the initial state particles undergo a "peripheral" collision, in which either the particles stay intact (elastic scattering), or they dissociate into low-mass states (diffractive dissociation). The scattered hadrons (or the low-mass states in the dissociative case) have energy equal, to within a few per cent, to that of the incoming hadron, and very small transverse momentum. Diffractive interactions can be parameterised in the framework of Regge phenomenology, where they are ascribed to the exchange of a trajectory with the vacuum quantum numbers, the Pomeron trajectory [1]. In the same framework, events in which the proton loses a more substantial fraction of its energy are ascribed to the exchange of subleading trajectories.

Significant progress has recently been made in understanding diffraction in terms of QCD, notably by studying the diffractive dissociation of virtual photons in electron-proton or positron-proton collisions at HERA. In fact, diffraction has proven to be a tool to study QCD and the low-x structure of the proton [2,3]. In the proton's rest frame, diffractive ep scattering, $ep \rightarrow eXp$, proceeds from the fluctuation of the virtual photon emitted by the electron (or by the positron) into a colour dipole, such as a quark-antiquark pair or a quark-antiquark-gluon system. The dipole interacts hadronically with the proton via the exchange of an object with vacuum quantum numbers – a gluon pair, in leadingorder QCD – and then dissociates into the hadronic state, X. The dipole has transverse dimensions which decrease as the photon virtuality, Q^2 , increases. It is thus possible to study diffractive interactions in a regime where one of the two interacting hadrons is so small that the strong interaction can be treated perturbatively. Alternatively, in a frame in which the proton is fast, the reaction can be seen as the deep inelastic scattering (DIS) of a pointlike virtual photon off the exchanged object. This gives access to the diffractive parton distribution functions (PDF), for which a QCD factorisation theorem has been proven [4–6]. Diffractive PDFs are defined as the proton PDFs probed when the vacuum quantum numbers are exchanged and the proton emerges intact from the interaction, suffering only a small energy loss. In the context of QCD, Pomeron exchange should then be understood as a synonym for exchange of partons from the proton with the vacuum quantum numbers.

This paper presents new measurements of the reaction $e^+p \to e^+Xp$ in the regions 0.03 $< Q^2 < 0.60 \text{ GeV}^2$ (low- Q^2 sample) and $2 < Q^2 < 100 \text{ GeV}^2$ (high- Q^2 sample) ¹. The measurements were made using the ZEUS detector at the HERA ep collider. The events were selected by requiring the detection in the ZEUS leading proton spectrometer (LPS) of a scattered proton, carrying a fraction x_L of the incoming proton momentum of at

 $^{^{1}}$ In the following, for simplicity, the symbol e will be used to denote both electrons and positrons.

least 0.9; such fast protons are referred to as leading. This x_L range includes the so-called diffractive peak, the narrow peak in the cross section at $x_L \approx 1$ ascribed to Pomeron exchange, as well as the transition to the lower x_L region in which subleading, mesonic exchanges, notably Reggeons, are thought to dominate [1,3]. The measurement covers the region $0.075 < |t| < 0.35 \text{ GeV}^2$, where t is the square of the four-momentum transferred at the proton vertex.

Sections 2-9 present the experimental set-up and the details of the analysis. Section 10 gives the results. The t and Φ dependences of the cross section are discussed first, where Φ is the azimuthal angle between the positron and the proton scattering planes in the $\gamma^* p$ rest frame. The distribution of Φ is sensitive to the interference between the amplitudes for scattering of longitudinally and transversely polarised photons, and thus to the helicity structure of the interaction. The Q^2 dependence of the photon-proton differential crosssection $d\sigma^{\gamma^*p\to Xp}/dM_X$ is then studied for different values of the photon-proton centre-ofmass energy, W. The data are also discussed in terms of the diffractive structure function, $F_2^{D(3)}$. The dependence of $F_2^{D(3)}$ on $x_{\mathbb{I}\!P}$ is studied, where $x_{\mathbb{I}\!P}$ is the fraction of the proton momentum carried by the object (the Pomeron or the Reggeon, in the Regge framework) exchanged between the virtual photon and the proton, $x_{\mathbb{P}} \simeq 1 - x_{\mathbb{L}}$. The Q^2 and β dependences of $F_2^{D(3)}$ for different values of $x_{\mathbb{P}}$ are investigated, and the behaviour of $F_2^{D(3)}$ is compared to that of the inclusive proton structure function, F_2 . The variable β is the Bjorken variable defined with respect to the four-momentum of the exchanged object. The results are compared to theoretical predictions based on the colour-dipole approach outlined above. Finally, a next-to-leading-order (NLO) QCD fit to the higher- Q^2 data is presented.

The present data correspond to an integrated luminosity about a factor four larger than that of the previous ZEUS-LPS analysis [7]. The low- Q^2 results have a wider Q^2 and W coverage than that studied so far with the LPS or other methods [7,8]. The Φ distribution is investigated for the first time. The cross section is measured up to M_X values of 40 GeV, so far unexplored, and $F_2^{D(3)}$ is presented up to $x_{\mathbb{P}}$ values of 0.07, thus covering the diffractive-peak region ($x_{\mathbb{P}} \lesssim 0.02$) and the transition to the non-diffractive region that is dominated by subleading exchanges.

It is also possible to select diffractive events without detecting the scattered proton. In a previous paper [9], a method based on features of the shape of the mass spectrum of the hadronic final-state X (M_X method) was applied. A discussion of the two approaches is presented, along with a comparison of the corresponding results.

2 Kinematics and cross sections

Figure 1 shows a schematic diagram of the process $ep \to eXp$. The kinematics of this reaction is described by the variables:

- $Q^2 = -q^2 = -(k k')^2$, the negative four-momentum squared of the virtual photon, where k(k') is the four-momentum of the incident (scattered) positron;
- $W^2 = (q+P)^2$, the squared centre-of-mass energy of the photon-proton system, where P is the four-momentum of the incident proton;
- $x = Q^2/(2P \cdot q)$, the fraction of the proton momentum carried by the quark struck by the virtual photon in the infinite momentum frame (the Bjorken variable);
- $M_X^2 = (q+P-P')^2$, the squared mass of the system X, where P' is the four-momentum of the scattered proton;
- $t = (P P')^2$, the squared four-momentum transfer at the proton vertex;
- Φ , the angle between the positron scattering plane and the proton scattering plane in the γ^*p centre-of-mass frame.

The variables Q^2 , W and x are related by $x = Q^2/(Q^2 + W^2 - M_p^2)$, where M_p is the proton mass.

The differential cross sections for the reactions $ep \to eXp$ and $\gamma^*p \to Xp$ are related by

$$\frac{d\sigma^{ep\to eXp}}{d\ln W^2 dQ^2 dM_X dt} = \frac{\alpha}{2\pi} \frac{1 + (1-y)^2}{Q^2} \frac{d(\sigma_T^{\gamma^* p\to Xp} + \sigma_L^{\gamma^* p\to Xp})}{dM_X dt} \left[1 - \frac{y^2}{1 + (1-y)^2} \frac{R^D}{1 + R^D} \right]
\simeq \frac{\alpha}{2\pi} \frac{1 + (1-y)^2}{Q^2} \frac{d\sigma^{\gamma^* p\to Xp}}{dM_X dt},$$
(1)

where α is the fine structure constant and $y = (P \cdot q)/(P \cdot k)$ is the fraction of the positron energy transferred to the proton in its rest frame. The quantity $R^D = \sigma_L^{\gamma^* p \to Xp}/\sigma_T^{\gamma^* p \to Xp}$ is the ratio of the cross sections for longitudinally and transversely polarised virtual photons. In the region covered by the present data, the term within the square brackets is taken to be unity since R^D is expected to be small [10].

The kinematics of the reaction $ep \to eXp$ can also be described by Q^2 , t and Φ , in conjunction with the two dimensionless variables $x_{\mathbb{P}}$ and β introduced in Section 1 given by

$$x_{\mathbb{P}} = \frac{(P - P') \cdot q}{P \cdot q} = \frac{Q^2 + M_X^2 - t}{Q^2 + W^2 - M_p^2},\tag{2}$$

$$\beta = \frac{Q^2}{2(P - P') \cdot q} = \frac{Q^2}{Q^2 + M_X^2 - t}.$$
 (3)

The quantities $x_{\mathbb{P}}$ and β are related to x by $x_{\mathbb{P}}\beta = x$.

The cross section for the reaction $ep \to eXp$ can be expressed in terms of the structure function $F_2^{D(4)}$, which is defined by the equation

$$\frac{d\sigma^{ep\to eXp}}{d\beta dQ^{2}dx_{\mathbb{P}}dt} = \frac{4\pi\alpha^{2}}{\beta Q^{4}} \left[1 - y + \frac{y^{2}}{2(1+R^{D})} \right] F_{2}^{D(4)}(\beta, Q^{2}, x_{\mathbb{P}}, t)
\simeq \frac{4\pi\alpha^{2}}{\beta Q^{4}} \left[1 - y + \frac{y^{2}}{2} \right] F_{2}^{D(4)}(\beta, Q^{2}, x_{\mathbb{P}}, t).$$
(4)

The structure function $F_2^{D(3)}(\beta, Q^2, x_{\mathbb{P}})$ is obtained by integrating $F_2^{D(4)}$ over t:

$$F_2^{D(3)}(\beta, Q^2, x_{\mathbb{I}P}) = \int F_2^{D(4)}(\beta, Q^2, x_{\mathbb{I}P}, t) dt.$$

For the results presented in this paper, the integration was performed in the range $0 < |t| < 1 \text{ GeV}^2$.

For unpolarised positrons and protons, the cross section can also be decomposed as

$$\frac{d\sigma^{ep\to eXp}}{d\Phi} \propto \sigma_T^{\gamma^*p\to Xp} + \epsilon \sigma_L^{\gamma^*p\to Xp} - 2\sqrt{\epsilon(1+\epsilon)}\sigma_{LT}^{\gamma^*p\to Xp}\cos\Phi - \epsilon \sigma_{TT}^{\gamma^*p\to Xp}\cos2\Phi, \quad (5)$$

where $\sigma_{LT}^{\gamma^*p\to Xp}$ is the interference term between the amplitudes for longitudinal and transverse photons and $\sigma_{TT}^{\gamma^*p\to Xp}$ is the interference term between the amplitudes for the two transverse polarisations. The polarisation parameter ϵ is defined as $\epsilon = 2(1-y)/[1+(1-y)^2]$.

3 Selection of diffraction at HERA

The kinematics of diffractive scattering, $\gamma^* p \to Xp$, implies that three features should be present in the final state:

- 1. the proton suffers only a small perturbation and emerges from the interaction carrying a large fraction, x_L , of the incoming proton momentum. Diffractive events appear as a peak at $x_L \approx 1$, the diffractive peak, which at HERA approximately covers the region $0.98 < x_L < 1$. The absolute value of the four-momentum transfer squared t is typically much smaller than 1 GeV², with $\langle |t| \rangle \approx 0.15$ GeV²;
- 2. conservation of momentum implies that any other produced system (X) must have a small mass (M_X) with respect to the photon-proton centre-of-mass energy (since $1 x_L \gtrsim M_X^2/W^2$);
- 3. the difference in rapidity between the outgoing proton and the system X is $\Delta \eta \approx \ln(1/x_{\mathbb{IP}})$ [3]. This, combined with the peaking of the cross section at small values of $x_{\mathbb{IP}}$, leads to a large separation in rapidity between the outgoing proton and any other hadronic activity in the event.

There are two basic ways to select inclusive diffractive events. The first is the proton-tagging method (exploiting the first signature above), used in the present study and in earlier ones [7,8,11-13]. The second exploits the different characteristics of the system X in diffractive and non-diffractive events:

- in non-diffractive DIS, both the hadronic system associated with the struck quark, which is largely measured in the detector, and that of the proton remnant, which largely escapes down the beam-pipe, are coloured states. In this case, the distribution of the final-state particles is governed by conventional QCD fragmentation and particles are expected to be emitted uniformly in rapidity along the γ^* -p axis. This leads to a suppression of rapidity gaps as well as a suppression of small masses of the hadronic system observed in the detector;
- in contrast, small masses of the system X and large rapidity gaps are signatures of diffractive processes (the second and third signatures above). At HERA, diffractive analyses based on the hadronic methods have been made with event selections based both on the presence of large rapidity gaps (rapidity-gap method, see e.g. [2, 14] and references therein) and small masses of the system X (M_X method) [7,9].

The two basic approaches for the selection of diffractive events, the proton-tagging method and the hadronic methods, are complementary:

- in the hadronic methods, high M_X values are not accessible since the non-diffractive background grows with M_X . Also, the estimation of the non-diffractive background relies on models of fragmentation. Furthermore, the measured cross section includes a contribution from proton-dissociative events, $ep \to eXN$. In these events, the mass of the forward system (N) enters as another variable, and the observed particles must be assigned either to the system N or X. The number of events in which no particle from N is observed must be estimated from a Monte Carlo simulation. While these limitations add to the systematic uncertainty of the hadronic methods, the statistical precision of the results tends to be good due to the high acceptance of the central detector. Also, the acceptance is not limited in t, although no measurement of t is possible;
- conversely, samples selected in the proton-tagging method have little or no background from proton-dissociative events or from non-diffractive DIS. They also allow a direct measurement of the variables t, Φ and $x_{\mathbb{P}}$ (at large values of $x_{\mathbb{P}}$), and give access to higher values of M_X . The statistical precision, however, is poorer than for the results obtained using hadronic methods due to the small acceptance of the LPS approximately 2% in the diffractive peak region.

Section 10.5 presents a comparison between the results obtained with the LPS and M_X methods. The results are also compared to measurements made by the H1 collabora-

tion [14] in which diffraction was selected with the rapidity-gap method.

4 Experimental set-up

The measurements were carried out at the HERA collider in 1997 using the ZEUS detector. At that time, HERA operated with 820 GeV protons and 27.5 GeV positrons. The data used in this analysis correspond to integrated luminosities of $3.60 \pm 0.06 \text{ pb}^{-1}$ (low- Q^2 sample) and $12.8 \pm 0.2 \text{ pb}^{-1}$ (high- Q^2 sample).

A detailed description of the ZEUS detector can be found elsewhere [15]. A brief outline of the components that are most relevant for this analysis is given below.

Charged particles are tracked in the central tracking detector (CTD) [16], which operates in a magnetic field of 1.43 T provided by a thin superconducting coil. The CTD consists of 72 cylindrical drift chamber layers, organised in nine superlayers covering the polar-angle² region $15^{\circ} < \theta < 164^{\circ}$. The transverse-momentum resolution for full-length tracks is $\sigma(p_T)/p_T = 0.0058p_T \oplus 0.0065 \oplus 0.0014/p_T$, with p_T in GeV.

The high-resolution uranium-scintillator calorimeter (CAL) [17] consists of three parts: the forward (FCAL), the barrel (BCAL) and the rear (RCAL) calorimeters. The CAL energy resolutions, as measured under test beam conditions, are $\sigma(E)/E = 0.18/\sqrt{E}$ for electrons and $\sigma(E)/E = 0.35/\sqrt{E}$ for hadrons (E in GeV).

Low- Q^2 events were selected by identifying and measuring the scattered positron in the beam-pipe calorimeter (BPC) [18] and beam-pipe tracker (BPT) [19]. The BPC was a tungsten-scintillator sampling calorimeter, located 3 m from the interaction point and covered positron scattering angles relative to the incident direction of 15 to 34 mrad. The BPT was a silicon-microstrip tracking device situated immediately in front the BPC. In 1997, it was equipped with two detector planes to measure the X coordinate.

For the high- Q^2 sample, the impact point of the scattered positron was determined with the small-angle rear tracking detector (SRTD) [20] or the CAL. The SRTD is attached to the front face of the RCAL and consists of two planes of scintillator strips, 1 cm wide and 0.5 cm thick, arranged in orthogonal orientations and read out via optical fibres and photomultiplier tubes. It covers a region 68×68 cm² in X and Y, excluding a 10×20 cm² hole at the centre for the beam-pipe. The corresponding angular coverage is between 4° and 18° around the beam-pipe. Ambiguities in SRTD hits were resolved with the help of the hadron-electron separator (HES) [21], which consists of a layer of 10 000,

² The ZEUS coordinate system is a right-handed Cartesian system, with the Z axis pointing in the proton beam direction, referred to as the "forward direction", and the X axis pointing left towards the centre of HERA. The coordinate origin is at the nominal interaction point.

 $2.89 \times 3.05 \text{ cm}^2$ silicon-pad detectors inserted in the CAL at a depth of 3.3 radiation lengths.

The LPS [22] detected positively charged particles scattered at small angles and carrying a substantial fraction, x_L , of the incoming proton momentum; these particles remain in the beam-pipe and their trajectory was measured by a system of silicon microstrip detectors that could be inserted very close (typically a few mm) to the proton beam. The detectors were grouped in six stations, S1 to S6, placed along the beam line in the direction of the proton beam, between 23.8 m and 90.0 m from the interaction point. The particle deflections induced by the magnets of the proton beam-line allowed a momentum analysis of the scattered proton. For the present measurements, only stations S4, S5 and S6 were used. The resolutions were about 0.5% on the longitudinal momentum and about 5 MeV on the transverse momentum. The effective transverse-momentum resolution is dominated by the intrinsic transverse-momentum spread of the proton beam at the interaction point, which is about 40 MeV in the horizontal plane and about 90 MeV in the vertical plane. The LPS acceptance is approximately 2% and x_L -independent in the diffractive-peak region, $0.98 < x_L < 1$; it increases smoothly to about 10% as x_L decreases to 0.9.

The luminosity was measured from the rate of the bremsstrahlung process $ep \to e\gamma p$. The photon was measured in a lead-scintillator calorimeter [23] placed in the HERA tunnel at Z = -107 m.

5 Reconstruction of the kinematic variables

In the low- Q^2 analysis, $0.03 < Q^2 < 0.60 \,\mathrm{GeV^2}$, the scattered positron was measured in the BPC/BPT. The energy and angle of the scattered positron were used ("electron method") to determine Q^2 and W. For the high- Q^2 data ($2 < Q^2 < 100 \,\mathrm{GeV^2}$) the identification of the scattered positron was based on a neural network [24] which uses information from the CAL. The variables W and Q^2 were reconstructed using a combination of the electron method and the double angle method [25].

The longitudinal (p_Z) and transverse (p_X, p_Y) momenta of the scattered proton were measured with the LPS. The fractional energy of the outgoing proton, x_L , was defined as $x_L = p_Z/E_p$, where E_p is the incoming proton energy. The variable t is given by

$$t = -\frac{p_T^2}{x_L} - \frac{(1 - x_L)^2}{x_L} M_p^2, \tag{6}$$

where p_T is the transverse momentum of the proton with respect to the incoming beam direction. The t resolution is approximately $\sigma(|t|) = 0.14 \text{ GeV} \sqrt{|t|}$ (t in GeV²) and is dominated by the angular spread of the beam. The proton and the positron momenta

were used to determine Φ , the azimuthal angle between the positron and proton scattering planes in the γ^*p frame. The resolution on Φ is approximately 0.2 rad.

The four-momentum of the system X was determined from calorimeter and tracking information. The energy deposits in the CAL and the track momenta measured in the CTD were combined in energy flow objects (EFOs) [9,26] to obtain the best momentum resolution. The mass M_X was evaluated as

$$M_{X,EFO}^2 = \left(\sum E_i\right)^2 - \left(\sum p_{Xi}\right)^2 - \left(\sum p_{Yi}\right)^2 - \left(\sum p_{Zi}\right)^2,$$

where the sums run over all EFOs not assigned to the scattered positron. The mass M_X can also be determined from the outgoing proton momentum as reconstructed in the LPS:

$$M_{X,LPS}^2 \approx [1 - x_L(1+x)]W^2.$$

The best resolution on M_X is obtained with $M_{X,EFO}$ when M_X is small and with $M_{X,LPS}$ for large values of M_X , so M_X was reconstructed as

$$M_X^2 = w_{EFO} M_{X,EFO}^2 + w_{LPS} M_{X,LPS}^2, (7)$$

where the weights w_{EFO} and w_{LPS} are inversely proportional to the appropriate resolutions, and $w_{EFO} + w_{LPS} = 1$. The resulting resolution is $\sigma(M_X)/M_X = 0.35/\sqrt{M_X} + 0.08$, with M_X in GeV.

The variables $x_{\mathbb{P}}$ and β were obtained from Eqs. (2) and (3), using the value of M_X from Eq. (7). For the determination of $x_{\mathbb{P}}$, this procedure is equivalent, at large M_X , to evaluating $x_{\mathbb{P}}$ as $x_{\mathbb{P}} = 1 - x_L$.

The variable y was reconstructed as $y_{JB} = \sum \frac{(E_i - p_{Zi})_{had}}{2E_e}$, where the sum is over all EFOs not associated to the scattered positron and E_e is the energy of the incident positron ("Jacquet-Blondel method" [27]).

6 Event selection

The data used for the analysis were selected at the trigger level by requiring the presence of a scattered positron in the BPC or CAL and a scattered proton in the LPS. In the offline selection the following cuts were imposed, closely following those used in the F_2 analyses at low Q^2 [19] and high Q^2 [28]:

• the energy of the scattered positron, if measured in the BPC, was required to be between 3 and 7 GeV for the events with W > 260 GeV and greater than 7 GeV for

W < 260 GeV, reflecting the trigger selection. If measured in the CAL, the scattered positron energy was required to be larger than 10 GeV.

The position of the scattered positron was required to be within the fiducial regions of the BPC or the CAL. In addition, in case the positron was found in the BPC, the impact position at the BPC front face, as extrapolated from the BPT measurement, was required to match with that of the BPC shower. Furthermore, in order to identify electromagnetic showers and to reject hadrons, the transverse size (energy weighted root mean square) of the shower in the BPC was required to be less than 0.8 cm;

- the requirements $30 < (E p_Z) < 65$ GeV and $40 < (E p_Z) < 65$ GeV were imposed for the low- and high- Q^2 samples, respectively, where $E p_Z = \sum (E_i p_{Zi})$ and the summation runs over the energies and longitudinal momenta of the final-state positron and all EFOs. This cut reduces the size of the QED radiative corrections and the photoproduction background, i.e. the $Q^2 \approx 0$ events where the scattered positron escapes undetected in the rear beam-hole;
- in order to limit event migrations from low y, the variable y_{JB} was required to be greater than 0.06;
- the Z coordinate of the interaction vertex was required to be in the range -90 < Z < 90 cm for the low- Q^2 sample and -50 < Z < 50 cm for the high- Q^2 sample. Events without a vertex reconstructed using BPT tracks were discarded in the low- Q^2 analysis. In the high- Q^2 sample, events without a measured vertex were assigned to the nominal interaction point.

The following requirements were used to select the scattered proton measured in the LPS:

- the candidate proton was tracked along the beam line and was rejected if, at any point, the distance of approach to the beam pipe was less than 0.2 cm for $p_X < 0$, or less than 0.3 cm for $p_X > 0$. This cut reduces the sensitivity of the acceptance to the uncertainty in the position of the beam-pipe apertures;
- the variable t was required to be in the range $0.075 < |t| < 0.35 \text{ GeV}^2$. This cut eliminated regions where the LPS acceptance was small or rapidly changing;
- beam-halo background is caused by scattered protons, with energy close to that of the beam, originating from the interaction of a beam proton with the residual gas in the beam-pipe or with the beam collimators. A beam-halo proton may overlap with a standard non-diffractive DIS event. In this case, the proton measured in the LPS is uncorrelated with the activity in the central ZEUS detector. This background was suppressed by the requirement that the sum of the energy and the longitudinal component of the total momentum measured in the CAL, the BPC and the LPS be less than the kinematic limit of twice the incoming proton energy: $E + p_Z =$

 $(E+p_Z)_{\rm CAL}+(E+p_Z)_{\rm BPC}+2p_Z^{\rm LPS}<1655$ GeV. This cut takes into account the resolution of the measurement of $p_Z^{\rm LPS}$. The residual beam-halo background and its subtraction are discussed in Section 7.

The low- Q^2 analysis was further limited to the kinematic region $0.03 < Q^2 < 0.6 \text{ GeV}^2$, 63 < W < 280 GeV, $M_X > 1.5 \text{ GeV}$ and $x_L > 0.9$. The average Q^2 value for this sample is 0.23 GeV^2 . The high- Q^2 analysis was restricted to $2 < Q^2 < 100 \text{ GeV}^2$, 25 < W < 240 GeV, $M_X > 1.5 \text{ GeV}$ and $x_{I\!P} < 0.07$; the average Q^2 value is 10.5 GeV^2 . These selections yielded 334 events in the low- Q^2 sample and 5945 events in the high- Q^2 sample.

7 Monte Carlo simulation and acceptance corrections

Monte Carlo simulations were used to correct the data for acceptance and detector effects. In the low- Q^2 analysis, events of the type $ep \to eXp$ were simulated with the generator EPSOFT 2.0 [29,30], based on the triple-Regge formalism [1,3], in which the cross section can be expressed in terms of three trajectories. If all the trajectories are Pomerons (\mathbb{PPPP}) , the cross-section $d\sigma^{\gamma^*p\to Xp}/dM_X^2$ is approximately proportional to $1/M_X^2$. If one of the trajectories is a Reggeon (\mathbb{PPPR}) , the cross-section $d\sigma^{\gamma^*p\to Xp}/dM_X^2$ falls as $\sim 1/M_X^3$.

In the high- Q^2 analysis, the reaction $ep \to eXp$ was modelled with RAPGAP 2.08/06 [31], which is based on the model of Ingelman and Schlein [32]. In RAPGAP, the structure function $F_2^{D(4)}$ is expressed as the sum of Pomeron and Reggeon contributions:

$$F_2^{D(4)}(x_{\mathbb{I}\!P}, t, \beta, Q^2) = f_{\mathbb{I}\!P}(x_{\mathbb{I}\!P}, t) F_2^{\mathbb{I}\!P}(\beta, Q^2) + f_{\mathbb{I}\!R}(x_{\mathbb{I}\!P}, t) F_2^{\mathbb{I}\!R}(\beta, Q^2). \tag{8}$$

The Pomeron and Reggeon fluxes, $f_{\mathbb{P},\mathbb{R}}(x_{\mathbb{P}},t)$, were parameterised [1] as

$$f_{I\!P,I\!R}(x_{I\!P},t) = \frac{e^{b_0^{I\!P,I\!R}t}}{x_{I\!P}^{2\alpha_{I\!P,I\!R}(t)-1}},$$
 (9)

with linear trajectories $\alpha_{I\!\!P,R}(t) = \alpha_{I\!\!P,R}(0) + \alpha'_{I\!\!P,R}t$, and the values of the parameters were taken from hadron-hadron data. The Pomeron structure function $F_2^{I\!\!P}(\beta,Q^2)$ was taken from the H1 measurements [14] (fit 2). The Reggeon trajectory includes the ρ , the ω , the f_2 and a_2 mesons. Their structure functions are unknown and were approximated with that of the pion [33]. The assumption that $F_2^{D(3)}$ can be expressed as the product of a flux, depending only on $x_{I\!\!P}$ and t, and the structure function of a particle-like object (see Eq. (8)) is known as the "Regge factorisation" hypothesis. It gives a fair description of the data, although it has no justification in QCD, where only the concept of diffractive PDFs, which are functions of $(x_{I\!\!P}, t, \beta, Q^2)$, has a firm basis.

The Monte Carlo generator DIFFVM 1.0 [34] was used to simulate the double-dissociative reaction, $ep \rightarrow eXN$, where the proton diffractively dissociates into the state N.

Initial- and final-state QED radiation were simulated by using EPSOFT and RAPGAP in conjunction with HERACLES 4.6 [35].

The generated EPSOFT and RAPGAP events were reweighted in x_L and t so that the measured distributions were well described. All generated events were passed through the standard ZEUS detector simulation, based on the GEANT program [36], and the trigger simulation package. A comparison of data and MC simulations is presented in Figs. 2 and 3 for the variables x_L , t, Q^2 , W, M_X , and $x_{I\!\!P}$. In Figs. 2c and 2d, no LPS requirement was imposed, so as to reduce the statistical fluctuations. The simulations reproduce the data satisfactorily. The diffractive peak is evident in Figs. 2a and 3a.

In the low- Q^2 analysis, the measured number of events was corrected for acceptance binby-bin. Bin-centring corrections were applied in W, $x_{I\!\!P}$ and M_X assuming $\sigma^{\gamma^*p\to Xp} \propto W^{2(2\bar{\alpha}_{I\!\!P}-1)}$, $F_2^{D(3)} \propto 1/x_{I\!\!P}^{2\bar{\alpha}_{I\!\!P}-1}$, and $d\sigma^{\gamma^*p\to Xp}/dM_X^2 \propto 1/M_X^{2(2\bar{\alpha}_{I\!\!P}-1)}$, where $\bar{\alpha}_{I\!\!P}$ is the t-averaged value of the Pomeron trajectory as obtained from the present measurement (Section 10.6). In the high- Q^2 analysis, the cross section for the dissociation of virtual photons at a given point within a bin was obtained from the ratio of the measured number of events to the number of events in that bin predicted from the MC simulation, multiplied by the $\gamma^*p\to Xp$ cross section calculated by the Monte Carlo generator. Both the acceptance and the bin-centring corrections were thus taken from the MC simulation.

The cross section was directly measured only in a limited t region and extrapolated to $0 < |t| < 1 \text{ GeV}^2$ using the t dependence assumed in the Monte Carlo generator, which was reweighted to the measured value of b (see Section 10.1). The effect of the extrapolation is to increase the cross section by a factor of about two (to within 3%); this factor is largely independent of the measured kinematic variables. In the region covered by the present measurements, the extrapolation is performed assuming an exponential dependence on t, $d\sigma^{ep\to eXp}/dt \propto \exp(bt)$, with $b \simeq 7.9 \text{ GeV}^{-2}$ at low $x_{I\!\!P}$. Data from elastic and p-dissociative pp and $\bar{p}p$ scattering indicate that the t distribution is better described by the function $\exp(bt+ct^2)$. For example, fits to the $\bar{p}p$ data at $\sqrt{s}=546$ GeV [37] yield $c=2.3\pm0.1$ GeV⁻⁴. The present data are only weakly sensitive to the value of c. In the extrapolation to the range $0 < |t| < 1 \text{ GeV}^2$, c was taken to be zero, but was varied by up to 4 GeV^{-4} , yielding changes in the extrapolated cross section of up to 7%. This was included in the normalisation uncertainty discussed in Section 9.

The results presented in this paper were corrected to the Born level and to the following kinematic region:

• low- Q^2 data: $0.03 < Q^2 < 0.6 \text{ GeV}^2$, 63 < W < 280 GeV, $M_X > 1.5 \text{ GeV}$, $x_L > 0.9$ and $0 < |t| < 1 \text{ GeV}^2$;

• high- Q^2 data: $2 < Q^2 < 100 \text{ GeV}^2$, 25 < W < 240 GeV, $M_X > 1.5 \text{ GeV}$, $x_L > 0.9$ and $0 < |t| < 1 \text{ GeV}^2$.

8 Backgrounds

The main background contribution is given by proton beam-halo events. In such events, the proton detected in the LPS is not correlated with the measurements in the central detector. To estimate the size of this background, the variable $E + p_Z$ (see Section 6) was used. For a signal event, this quantity should be equal to twice the initial proton energy, 1640 GeV, whereas for a beam-halo event it can exceed this value.

The $E+p_Z$ spectrum for the beam-halo events was constructed as a random combination of generic DIS events (without the requirement of a track in the LPS) and a beam-halo track measured in the LPS. The resulting distribution, shown in Fig. 4 as the hatched histogram, was normalised to the data for $E+p_Z>1685$ GeV, which contain beam-halo events only (see Fig. 4). The background remaining after the $E+p_Z<1655$ GeV cut averaged $(10.2\pm0.7~(\text{stat.}))\%$ and was a function of $x_{I\!P}$ and t. All results presented in this paper were corrected for this background.

The contribution from proton-dissociative events, $ep \to eXN$, was studied with the Monte Carlo generator DIFFVM for the DIS sample and was found to be less than 4% in all bins. This contribution was neglected.

9 Systematic uncertainties

The systematic uncertainties were calculated by varying the cuts and by modifying the analysis procedure. The variations of the cuts were typically commensurate with the resolutions of the relevant variables, and in general the changes were similar to those made in earlier analyses [11, 12, 19, 22].

The following systematic checks were performed ³:

- to evaluate the uncertainties due to the measurement of the scattered positron:
 - low- Q^2 analysis: the checks performed in a previous publication [19] were repeated, and consistent results obtained. Since the present data are a subsample of those

³ The corresponding average effect on the cross section in the measured bins is indicated using the notation $_{-b}^{+a}$: given a systematic check which produces an increase of the cross section in some bins and a decrease in some other bins, a is the average increase and b is the average decrease.

- used earlier, the systematic uncertainties found previously [19] were used (typically smaller than $\pm 1.5\%$);
- high- Q^2 analysis: the fiducial region for the impact position of the positron was modified $\binom{+3.3}{-2.9}\%$; the minimum energy of the positron was increased to 12 GeV $\binom{+1.6}{-1.4}\%$;
- to evaluate the uncertainties due to the reconstruction of the final-state proton, the checks described below were performed. Consistent results were obtained for the low-and the high- Q^2 samples; because of the larger statistical fluctuations of the low- Q^2 sample, the uncertainties quoted are those determined from the high- Q^2 events;
 - the cut on the minimum distance of approach to the beam-pipe was increased by 0.03 cm ($^{+4.1}_{-2.4}\%$); the t range was enlarged to 0.07 < |t| < 0.4 GeV² ($^{+2.8}_{-1.1}\%$); the amount of the subtracted beam-halo background was varied by $\pm 20\%$ ($^{+2.0}_{-1.4}\%$);
- sensitivity to the other selection cuts:
 - low- Q^2 analysis: the checks performed in a previous publication [19] were repeated and consistent results found, notably for the sensitivity to the selections on y_{JB} , $E p_Z$ and the Z coordinate of the vertex. The systematic uncertainties determined in [19] were used (typically smaller than $\pm 1.5\%$);
 - high- Q^2 analysis: the minimum value of $E p_Z$ was raised to 45 GeV ($^{+1.3}_{-2.1}\%$); the cut on the Z coordinate of the vertex was restricted to -40 < Z < 40 cm ($^{+2.2}_{-1.3}\%$); the systematic error due to the uncertainty in the absolute calorimeter energy calibration was estimated by changing the energy scale by $\pm 2\%$ ($^{+2.6}_{-1.5}\%$); the minimum value of M_X was decreased to 1.3 GeV ($^{+1.7}_{-1.4}\%$);
- sensitivity to the Monte Carlo simulations:
 - low- Q^2 analysis: no reweighting of the x_L distribution was applied in the Monte Carlo simulation ($^{+3.2}_{-6.3}\%$); the value of the t slope was changed by $\pm 1.5 \text{ GeV}^{-2}$ ($^{+4.4}_{-0.7}\%$);
 - high- Q^2 analysis: the $x_{\mathbb{P}}$ distribution was reweighted by a factor $(1/x_{\mathbb{P}})^k$, with k varying between -0.05 and +0.05 $\binom{+1.7}{-1.1}$; the value of the t slope was changed by ± 1.5 GeV⁻² $\binom{+6.2}{-2.1}$; the Φ distribution was reweighted by a factor $(1 + k\cos\Phi)$, with k varying between -0.15 and +0.15 $\binom{+1.8}{-1.2}$; the intrinsic transverse-momentum spread of the proton beam at the interaction point was increased by 10 MeV in the horizontal plane and 20 MeV in the vertical plane $\binom{+2.7}{-2.1}$;
- the t slope was determined with an alternative method [22] based on expressing the measured t distribution as a convolution of an exponential distribution, $d\sigma/dt \propto e^{-b|t|}$, and a two-dimensional Gaussian distribution representing the transverse momentum distribution of the beam. This led to changes in the value of the t slope by up to +4%.

The total systematic uncertainty for each bin was determined by quadratically adding the individual contributions. The quoted uncertainties do not include an overall normalisation uncertainty of $\pm 10\%$ which originates mostly from the uncertainty of the simulation of the proton-beam optics; this uncertainty is largely independent of the kinematic variables and was therefore taken as a normalisation uncertainty. The $\pm 10\%$ normalisation uncertainty also includes the uncertainty on the integrated luminosity ($\pm 1.6\%$). In addition, a +7% uncertainty is present in the cross section and structure function results, except those for $d\sigma^{ep\to eXp}/dt$, due to the extrapolation from the measured t region to $0 < |t| < 1 \text{ GeV}^2$ (see Section 7). Thus the overall normalisation uncertainty is $\pm 10\%$.

10 Results

The results in this section are presented as follows. The differential cross-section $d\sigma^{ep\to eXp}/dt$ in the region $0.075 < |t| < 0.35 \text{ GeV}^2$ is presented first. The data are then integrated over t and extrapolated to the range $0 < |t| < 1 \text{ GeV}^2$, as discussed in Section 7. The resulting cross sections are presented as a function of Φ in Section 10.2, where the sensitivity of the present data to the helicity structure of the reaction $ep \to eXp$ is discussed. The dependence of the cross section on Q^2 is presented in Section 10.3, and is compared with that of the total photon-proton cross section.

In Section 10.4 the data are presented in terms of the diffractive structure function, $F_2^{D(3)}$. This allows an interpretation based on the diffractive PDFs of the proton. The present data in the diffractive-peak region are compared to those obtained with the M_X method by ZEUS and with the rapidity-gap method by H1 in Section 10.5.

In Section 10.6, the $x_{\mathbb{P}}$ dependence of $F_2^{D(3)}$ is used to extract the intercept of the Pomeron trajectory, $\alpha_{\mathbb{P}}(0)$, the quantity that, in Regge phenomenology, determines the energy dependence of the total hadron-hadron cross section [1]. It is interesting to see if the value of $\alpha_{\mathbb{P}}(0)$ in ep diffractive scattering at high Q^2 is larger than that measured in hadron-hadron collisions, as expected in the framework introduced earlier, in which diffraction is due to the exchange of partons from the proton. In Section 10.7 the results are compared to some perturbative QCD (pQCD) models based on the dipole picture outlined in Section 1. Finally, an NLO QCD fit was performed.

The results of this paper extend up to $x_{\mathbb{P}} \simeq 0.07$. In the following, the data for the diffractive-peak region are often contrasted with those at high $x_{\mathbb{P}}$. For this purpose, the value $x_{\mathbb{P}} = 0.01$ is chosen as the transition between the high- and low- $x_{\mathbb{P}}$ bins, such that the low- $x_{\mathbb{P}}$ bins are dominated by diffractive-peak events. This choice is somewhat restrictive, since the diffractive peak extends to $x_{\mathbb{P}} \simeq 0.02$, see Figs. 2a and 3a. In the

region $x_{\mathbb{P}} < 0.01$, the contribution from non-Pomeron exchanges is less than 10%. The average value of $x_{\mathbb{P}}$ is 0.003 for $x_{\mathbb{P}} < 0.01$ and 0.043 for $x_{\mathbb{P}} > 0.01$.

Preliminary versions of the present results, along with details of the analysis, have been presented earlier [38–40].

10.1 t dependence

Figure 5a presents the differential cross-section $d\sigma^{ep\to eXp}/dt$ in the kinematic range 2 < Q^2 < 100 GeV², M_X > 1.5 GeV, $x_{I\!\!P}$ < 0.01. For this sample, $\langle Q^2 \rangle = 8.4$ GeV² and $\langle \beta \rangle = 0.32$. The value of the slope parameter, b, obtained from the fit with the function $d\sigma^{ep\to eXp}/dt \propto e^{-b|t|}$ in the range 0.075 < |t| < 0.35 GeV² is

$$b = 7.9 \pm 0.5 \text{(stat.)}^{+0.9}_{-0.5} \text{(syst.)} \text{ GeV}^{-2}.$$

This agrees with and improves on the previous measurement of the diffractive slope of $b = 7.2 \pm 1.1(\text{stat.})^{+0.7}_{-0.9}(\text{syst.}) \text{ GeV}^{-2}$ [11].

The t distribution was studied in two Q^2 bins, $2 < Q^2 < 7 \text{ GeV}^2$ and $7 < Q^2 < 100 \text{ GeV}^2$. The fitted values of b are $7.7 \pm 0.7 (\text{stat.})^{+0.9}_{-0.7} (\text{syst.})$ GeV⁻² and $8.0 \pm 0.8 (\text{stat.})^{+0.9}_{-0.5} (\text{syst.})$ GeV⁻², respectively. These results, presented in Fig. 5b together with the previous ZEUS measurements in photoproduction [12] and in DIS [11], show that b is independent of Q^2 within the errors. This behaviour is expected in a QCD-based model [41].

However, the value of b decreases with $x_{\mathbb{P}}$, as shown in Fig. 5c (see also Table 1). Figure 5d shows the values of $b_{p_T^2}$ in bins of $x_{\mathbb{P}}$, calculated from the fit to $d\sigma^{ep\to eXp}/dp_T^2$, so that they can be compared with those of a previous ZEUS publication [8]. The relationship between t and p_T^2 is given in Eq. (6). In the region of the present data, the values of b and $b_{p_T^2}$ differ by less than their uncertainties. The present results are consistent with those of the previous ZEUS publication [8]. The p_T^2 slope reaches a minimum value for $x_{\mathbb{P}} \approx 0.05$ and then rises to $b_{p_T^2} \approx 7 \text{ GeV}^{-2}$ for higher $x_{\mathbb{P}}$ values.

In the dipole model, in which the virtual photon fluctuates into $q\bar{q}$ or $q\bar{q}g$ systems, the $q\bar{q}g$ contribution dominates for $\beta < 0.2$ -0.3 [3]. Different t dependences for the $q\bar{q}$ and $q\bar{q}g$ regions are expected [41], with slopes higher by up to 3 GeV⁻² at high β in the diffractive peak. In addition, in the $q\bar{q}g$ region, the slope b is expected to decrease logarithmically with $x_{I\!\!P}$: $b = b_0^{I\!\!P} - 2\alpha'_{I\!\!P} \ln x_{I\!\!P}$, the so-called shrinkage of the diffractive cone [3]. A decrease is observed in the data, and so is a significant β dependence. However, these dependences are visible only over an $x_{I\!\!P}$ range, $x_{I\!\!P} \lesssim 0.07$, that goes beyond the diffractive-peak region (Fig. 5c), making a comparison with the predictions inconclusive. At higher $x_{I\!\!P}$ values, a rise of b with $x_{I\!\!P}$ is predicted by a Regge-based model [42], though at a rate smaller than that observed in the data.

10.2 Azimuthal asymmetry

The azimuthal angle Φ between the positron and proton scattering planes is sensitive to the helicity structure of the reaction $ep \to eXp$, as shown explicitly in Eq. (5). The analysis of the azimuthal distribution is limited to the high- Q^2 data, since the statistics of the low- Q^2 sample is too small. For this part of the analysis, a radial cut of 18 cm was imposed on the impact point of the scattered electron at the RCAL surface, along with the restriction $Q^2 > 4$ GeV². This reduces the Φ dependence of the acceptance.

Figures 6a and 6b show the Φ distribution for the two ranges $0.00025 < x_{I\!\!P} < 0.01$ and $0.01 < x_{I\!\!P} < 0.07$. Here again, $x_{I\!\!P} = 0.01$ was chosen as the transition between the high-and low- $x_{I\!\!P}$ bins such that the low- $x_{I\!\!P}$ bin is dominated by diffractive-peak events. The distributions were fitted to the form

$$\frac{d\sigma^{ep\to eXp}}{d\Phi} \propto 1 + A_{LT}\cos\Phi + A_{TT}\cos2\Phi,$$

where A_{LT} and A_{TT} are proportional to $\sigma_{LT}^{\gamma^*p\to Xp}$ and $\sigma_{TT}^{\gamma^*p\to Xp}$, respectively. The values of the azimuthal asymmetries obtained in the fit are

$$A_{LT} = 0.009 \pm 0.073 (\text{stat.})^{+0.076}_{-0.039} (\text{syst.}),$$

 $A_{TT} = 0.005 \pm 0.074 (\text{stat.})^{+0.043}_{-0.074} (\text{syst.})$

and

$$A_{LT} = 0.007 \pm 0.048 (\text{stat.})^{+0.043}_{-0.071} (\text{syst.}),$$

 $A_{TT} = 0.019 \pm 0.046 (\text{stat.})^{+0.026}_{-0.053} (\text{syst.})$

for the ranges $0.00025 < x_{I\!\!P} < 0.01$ and $0.01 < x_{I\!\!P} < 0.07$, respectively. The interference terms between the longitudinal and transverse amplitudes and between the two transverse amplitudes thus appear to be small in the measured kinematic range, both in the diffractive-peak region and at higher $x_{I\!\!P}$ values, suggesting that the helicity structure of the reaction $ep \to eXp$ is similar for Pomeron and Reggeon exchanges.

Figure 6c presents A_{LT} as a function of $x_{\mathbb{P}}$ and Figs. 6d-f present A_{LT} as a function of β , t and Q^2 for $x_{\mathbb{P}} < 0.01$. The asymmetry is consistent with zero in all measured bins. The results are summarised in Table 2.

The measured value of A_{LT} can be compared with the results obtained in exclusive electroproduction of ρ^0 mesons, $ep \to e\rho^0 p$, in which the hadronic final state, X, consists of a ρ^0 meson only. In this case, $A_{LT} = -\sqrt{2\epsilon(1+\epsilon)} \cdot (r_{00}^5 + 2r_{11}^5) = -0.262 \pm 0.038 \text{(stat.)} \pm 0.068 \text{(syst.)}$, where r_{00}^5 and r_{11}^5 are two of the ρ^0 spin-density matrix elements [43]. The present data show that the asymmetry is smaller for inclusive scattering than for exclusive ρ^0 electroproduction.

There are numerous pQCD-based predictions for the behaviour of A_{LT} [44–47] in the diffractive peak, mostly concerning the high- β region ($\beta > 0.6$ -0.9), where the asymmetry is expected to be largest, reflecting the large expected value of $\sigma_L^{\gamma^*p\to Xp}$; this region was not accessible due to limited statistics. In all calculations, back-to-back configurations, i.e. $A_{LT} < 0$, are favoured; the asymmetry is expected to be close to zero at low β , in agreement with the present data.

The measurement of the Φ dependence can, in principle, be used to constrain the cross section of longitudinally polarised photons [45–47], a quantity notoriously difficult to extract unless data at different centre-of-mass energies are available. No experimental results on $\sigma_L^{\gamma^* p \to Xp}$ exist so far. The asymmetry A_{LT} can be related to R^D [47]; however, only for $\beta > 0.8$ -0.9, beyond the region covered by the present data, is the determination of R^D model-independent. More general limits can be obtained for $\sigma_L^{\gamma^* p \to Xp}$; using hermiticity and parity conservation, the following relations are found [45,46]:

$$\frac{2(\sigma_{LT}^{\gamma^*p \to Xp})^2}{\sigma_0 - \sigma_{TT}^{\gamma^*p \to Xp}} \le \sigma_L^{\gamma^*p \to Xp} \le \frac{\sigma_0 - \sigma_{TT}^{\gamma^*p \to Xp}}{\epsilon},\tag{10}$$

where $\sigma_0 = \sigma_T^{\gamma^* p \to Xp} + \epsilon \sigma_L^{\gamma^* p \to Xp}$. The larger the values of the interference terms $\sigma_{LT}^{\gamma^* p \to Xp}$ and $\sigma_{TT}^{\gamma^* p \to Xp}$, the stronger the constraint on $\sigma_L^{\gamma^* p \to Xp}$. The fact that in the present data the measured asymmetries A_{LT} and A_{TT} are consistent with zero implies that the interference terms $\sigma_{LT}^{\gamma^* p \to Xp}$ and $\sigma_{TT}^{\gamma^* p \to Xp}$ are also consistent with zero. In this case, the inequalities (10) are trivially satisfied and give no information on $\sigma_L^{\gamma^* p \to Xp}$.

$10.3 \quad Q^2 ext{ dependence of } d\sigma^{\gamma^\star p o Xp}/dM_X$

Figure 7 shows the cross-section $d\sigma^{\gamma^*p\to Xp}/dM_X$ as a function of Q^2 for different M_X and W values. The data are also presented in Tables 3 and 4. The present measurements are shown together with the previous ZEUS results at low [7] and high Q^2 [9]; the latter have been corrected for the residual double-dissociative background, taken to be 31%, as determined [9] by comparing those data with the LPS results [11] ⁴. The present results are consistent with the earlier ZEUS measurements [7,9] and cover a wider kinematic region; notably, they reach higher values of M_X , lower values of Q^2 , as well as values of W close to the kinematic limit. The points at $M_X = 5$ GeV are all in the diffractive-peak region, since $x_{\mathbb{P}} < 0.01$. The other bins have contributions from $x_{\mathbb{P}} > 0.01$. In all regions of $x_{\mathbb{P}}$, the data exhibit a behaviour qualitatively similar to that of the total γ^*p cross section, $\sigma^{\gamma^*p}_{\text{tot}}$: $d\sigma^{\gamma^*p\to Xp}/dM_X$ falls rapidly with Q^2 at high Q^2 ; as $Q^2 \to 0$, the cross-section dependence on Q^2 becomes weak, with $d\sigma^{\gamma^*p\to Xp}/dM_X$ approaching a constant, as expected from the

⁴ As discussed in Section 10.5, a higher fraction was measured at lower Q^2 [7].

conservation of the electromagnetic current. The behaviour of $d\sigma^{\gamma^*p\to Xp}/dM_X$ cannot be fitted with a simple, form-factor-like function of the type $1/(Q^2+M_X^2)^n$, but is described by a pQCD-based model [48] at $x_{\mathbb{P}} \lesssim 0.01$ and large Q^2 (see the continuous curves in Fig. 7). This model and the comparison between its predictions and the data, as well as the curves on Fig. 7, are discussed in Section 10.7.

A direct comparison between $d\sigma^{\gamma^*p\to Xp}/dM_X$ and the total photon-proton cross section is shown in Fig. 8, where the ratio $(M_X^2 d\sigma^{\gamma^*p\to Xp}/dM_X^2)/\sigma_{\text{tot}}^{\gamma^*p}$ is presented as a function of Q^2 at different M_X and W values. The values of the γ^*p total cross section were obtained from the ALLM97 parameterisation [49], which is consistent with the latest H1 and ZEUS F_2 data [50]. The plot shows that, in spite of their qualitative similarity, $d\sigma^{\gamma^*p\to Xp}/dM_X$ and the total cross section exhibit some differences in their Q^2 dependences. In the bin at $M_X = 5$ GeV, which has data from the diffractive peak region only, the ratio grows slowly with Q^2 for $Q^2 < M_X^2$ and then falls in the region dominated by $q\bar{q}$ fluctuations of the photon. At higher M_X values, which correspond to $x_{\mathbb{P}}$ larger than 0.01, Q^2 is always smaller than M_X^2 and the ratio grows, indicating a softer Q^2 dependence of $d\sigma^{\gamma^*p\to Xp}/dM_X^2$ than of $\sigma_{\text{tot}}^{\gamma^*p}$. Here again, the low- $x_{\mathbb{P}}$ data in the high- Q^2 region can be described by pQCD-based models of diffraction, as argued in Section 10.7, where the curves on Fig. 8 are discussed.

10.4 The structure function $F_2^{D(3)}$

The data of Fig. 7 are presented in Fig. 9 (see also Tables 5-9) in terms of the structure function $F_2^{D(3)}$, evaluated under the assumption that $R^D = 0$. As discussed in Section 2, $F_2^{D(3)}$ is defined in this paper as the integral of $F_2^{D(4)}$ over the range $0 < |t| < 1 \text{ GeV}^2$. The figure shows $x_{\mathbb{P}}F_2^{D(3)}(\beta, Q^2, x_{\mathbb{P}})$ as a function of $x_{\mathbb{P}}$ for different values of β and Q^2 . In order to maximise the kinematic overlap between the low- Q^2 and the high- Q^2 samples, only a subset of the low- Q^2 sample is presented in Fig. 9 and Table 5. The values of $x_{\mathbb{P}}F_2^{D(3)}$ decrease with $x_{\mathbb{P}}$ at small $x_{\mathbb{P}}$, indicating that $F_2^{D(3)}$ falls with $x_{\mathbb{P}}$ faster than $1/x_{\mathbb{P}}$. At larger $x_{\mathbb{P}}$, $x_{\mathbb{P}}F_2^{D(3)}$ flattens and, in some bins, increases with $x_{\mathbb{P}}$, indicating a softer dependence of $F_2^{D(3)}$ on $x_{\mathbb{P}}$. The $x_{\mathbb{P}}$ dependence can be parameterised in terms of the Pomeron intercept $\alpha_{\mathbb{P}}(0)$. The extraction of $\alpha_{\mathbb{P}}(0)$ is presented in Section 10.6, where the curves in Fig. 9 are discussed.

The dependences of the structure function on Q^2 and β are presented in Figs. 10-12 for different values of $x_{\mathbb{P}}$. The structure function rises with Q^2 in all of the explored kinematic region. Figure 10 compares the low- Q^2 and high- Q^2 results in the $x_{\mathbb{P}}$ - β region where they overlap. Between the low- and high- Q^2 data, i.e. between $\langle Q^2 \rangle \simeq 0.15 \text{ GeV}^2$ and $\langle Q^2 \rangle \simeq 10.5 \text{ GeV}^2$, the increase is about a factor five; this steep rise, $F_2^D \propto Q^2$, reflects the flattening of $d\sigma^{\gamma^*p\to Xp}/dM_X$ for $Q^2\to 0$ (see Eqs. (1), (4)), and is a consequence of

the conservation of the electromagnetic current. The Q^2 dependence becomes slower in the high- Q^2 data (Fig. 11). In this region, the rise can be interpreted as a manifestation of QCD evolution; these positive scaling violations are due to the large gluon contribution to F_2^D (see Section 10.7.3). The behaviour is similar in all $x_{\mathbb{P}}$ bins, both in the diffractive peak region and at larger $x_{\mathbb{P}}$ values, suggesting that the QCD evolution of the diffractive PDFs is largely independent of $x_{\mathbb{P}}$. The β dependence of $F_2^{D(3)}$ (Fig. 12) has instead a different behaviour at different values of $x_{\mathbb{P}}$: at small $x_{\mathbb{P}}$, $F_2^{D(3)}$ has a weak β dependence with a tendency to rise at large values of β ; for $x_{\mathbb{P}} \gtrsim 0.02$, $F_2^{D(3)}$ decreases as β approaches unity, as expected in a hadron (bearing in mind that β is the equivalent of Bjorken-x for the exchange). The solid curves shown on Figs. 11 and 12 are the predictions from a pQCD-based model [51] valid in the diffractive region and discussed in Section 10.7.2.

The structure function $F_2^{D(3)}$ and the inclusive proton structure function F_2 are compared in terms of the ratio $x_{\mathbb{P}}F_2^{D(3)}(x_{\mathbb{P}},x,Q^2)/F_2(x,Q^2)$ calculated at fixed values of $x_{\mathbb{P}}$. The values of $F_2(x,Q^2)$ were obtained from the ALLM97 parameterisation. The ratio is presented in Figs. 13 and 14 as a function of Q^2 and x, respectively. The x range covered by the data is $5 \times 10^{-5} \lesssim x \lesssim 5 \times 10^{-2}$. The ratio is largely Q^2 -independent, with possibly some structure at high β and low $x_{\mathbb{P}}$. A Q^2 -independent ratio would indicate equal scaling violations in the proton for the reaction $\gamma^*p \to Xp$ and for inclusive DIS. The ratio grows with x in the diffractive-peak region, suggesting that the x dependence of the proton PDFs is different when the proton is probed in $\gamma^*p \to Xp$ and in inclusive DIS. At higher $x_{\mathbb{P}}$, $x_{\mathbb{P}} \gtrsim 0.02$, the ratio becomes flatter.

10.5 Comparison with the results of the M_X method and of H1

In this section, the present results are compared with those obtained with the M_X method [9] and with the H1 results obtained with the rapidity-gap technique [14].

The M_X -method analysis [9] includes events in which the proton diffractively dissociates into a system N of mass $M_N \lesssim 5.5$ GeV. In order to facilitate the comparison, the present data were replotted using the binning of the M_X -method publication [9].

The M_X -method points are higher than those obtained with the LPS method. The difference was quantified by means of BEKW-type fits to the two data sets (see Section 10.7.1), which give a ratio of the M_X -method to LPS points of $R_{M_X} = 1.55 \pm 0.08^{+0.15}_{-0.17}$, where the first error includes the statistical and systematic uncertainties and the second is due to the normalisation uncertainty. Figure 15 shows $x_P F_2^{D(3)}$ for the two data sets after scaling down the M_X -method points by R_{M_X} . The agreement between the LPS points and the renormalised M_X -method results is good, indicating that the difference is mainly in the normalisation. The normalisation difference can be attributed to the residual p-dissociative background in the M_X method. This background was estimated in previous

studies [9] by comparing the M_X results [9] and the earlier LPS data [11]; there the ratio R_{M_X} was found to be $R_{M_X} = 1.45^{+0.34}_{-0.23}$, consistent with the present result. A similar study was performed [7] for the BPC region, resulting in $R_{M_X} = 1.85 \pm 0.38$ (stat.), which is also consistent with the present measurement. The measured value of R_{M_X} corresponds to a percentage of p-dissociative events in the sample of $R_{\text{diss}} = (1-1/R_{M_X}) = [35.5 \pm 3.3^{+6.2}_{-7.1}]\%$; the first error corresponds to the statistical and systematic uncertainties in quadrature, the second is due to the normalisation uncertainty.

The agreement between the LPS and the M_X -method results, after taking the protondissociative background into account, lends support to the assumptions on which the M_X method is based.

Figure 16 shows a comparison of the present $F_2^{D(3)}$ results with those of the H1 collaboration obtained with the rapidity-gap selection [14]. These data include a p-dissociative contribution with $M_N < 1.6$ GeV. The data are plotted in terms of $x_{\mathbb{P}}F_2^{D(3)}$ as a function of $x_{\mathbb{P}}$ in different β and Q^2 bins. The ZEUS points were extrapolated to the H1 bin centres using the measured dependences. At small $x_{\mathbb{P}}$, $x_{\mathbb{P}} < 0.01$, the agreement is good, although with a tendency for the H1 points to be higher than the present results at high Q^2 . While a normalisation difference is consistent with the presence of a p-dissociative contribution in the H1 data, a Q^2 dependence of this difference is not expected. The comparison indicates that the H1 data have a stronger Q^2 dependence than the present data. For $x_{\mathbb{P}} > 0.01$, the H1 data are also higher, but the shape is somewhat different, with a larger Reggeon-like contribution in the H1 data.

10.6 Extraction of the Pomeron intercept

In the framework of Regge phenomenology, the $x_{I\!\!P}$ dependence of $F_2^{D(3)}$ is related to the intercept of the Pomeron trajectory, the parameter that drives the energy dependence of the total hadron-hadron cross section at high energies [3]. The Pomeron intercept has been determined to be $1.0964^{+0.0115}_{-0.0091}$ [52] in soft hadronic interactions. However, the same parameter is significantly larger in the diffractive production of heavy vector mesons, notably in J/ψ photoproduction (see e.g. [2]), reflecting the rapid rise of the cross section with W. This is a consequence of the increase of the parton densities in the proton at low x, which drives the rise of the cross section with decreasing x, and hence with decreasing $x_{I\!\!P}$ (since $x_{I\!\!P} \propto 1/W^2 \propto x$). It is interesting to determine if such a deviation from the behaviour of the hadron-hadron data is also apparent in the inclusive diffractive dissociation of virtual photons.

The high- Q^2 data of Fig. 9 with $x_{\mathbb{P}} < 0.01$ were fitted to the form:

$$F_2^{D(3)}(\beta,Q^2,x_{I\!\!P}) = f_{I\!\!P}(x_{I\!\!P}) \cdot F_2^{I\!\!P}(\beta,Q^2),$$

i.e. assuming "Regge factorisation" (see Section 7). The Pomeron flux was parameterised as [1]

$$f_{\mathbb{P}}(x_{\mathbb{P}}) = \int \frac{e^{b_0^{\mathbb{P}}t}}{x_{\mathbb{P}}^{2\alpha_{\mathbb{P}}(t)-1}} dt.$$

The parameter $\alpha_{I\!\!P}'$ was set to 0.25 GeV⁻², consistent with the hadron-hadron data [53]. The parameter $b_0^{I\!\!P}$ was taken to be 4.67 GeV⁻², such that the relation $b = b_0^{I\!\!P} - 2\alpha_{I\!\!P}' \ln x_{I\!\!P}$ [3] reproduces the results of Section 10.1. The values of $F_2^{I\!\!P}(\beta,Q^2)$ in each β and Q^2 bin and the Pomeron intercept (assumed to be β and Q^2 independent) were treated as free parameters. The resulting Pomeron intercept is

$$\alpha_{I\!\!P}(0) = 1.16 \pm 0.02 \text{ (stat.)} \pm 0.02 \text{ (syst.)}.$$

Varying $\alpha'_{I\!\!P}$ in the range $0 < \alpha'_{I\!\!P} < 0.4 \; {\rm GeV^{-2}}$ causes $\alpha_{I\!\!P}(0)$ to change by $^{+0.011}_{-0.030}$; the chosen range includes the small values of $\alpha_{\mathbb{P}}$ measured in the diffractive photoproduction of J/ψ mesons [54]. A variation of \mathbb{R}^D between 0 and 1 produces a change of $\alpha_{\mathbb{P}}(0)$ of +0.017. The quality of the fit is good, with $\chi^2/ndf = 14.2/22$ (considering statistical uncertainties only). The fact that the same value of $\alpha_{\mathbb{P}}(0)$ fits the whole Q^2 , β region covered by the data indicates that, within the present accuracy, the hypothesis of Regge factorisation is a good approximation. The result does not change if the fit is extended to the low- Q^2 region; in this case $\chi^2/ndf = 14.6/28$ (statistical uncertainties only). The result of this latter fit is shown in Fig. 9. The extrapolation of the fit for $x_{\mathbb{P}} > 0.01$, where the contribution from the exchange of the Reggeon trajectory becomes important, is also shown; indeed the fit does not describe this region satisfactorily. The present value of $\alpha_{\mathbb{P}}(0)$ is consistent with that from H1, $\alpha_{I\!\!P}(0) = 1.203 \pm 0.020 ({\rm stat.}) \pm 0.013 ({\rm syst.})^{+0.030}_{-0.035} ({\rm model})$ (measured in the region 4.5 $< Q^2 < 75 \text{ GeV}^2$) [14], and with the earlier ZEUS result, $\alpha_{\mathbb{P}}(0) =$ $1.157 \pm 0.009 (\text{stat.})^{+0.039}_{-0.012} (\text{syst.})$ (measured in the region $7 < Q^2 < 140 \text{ GeV}^2$) [9]; it is higher than that of the soft Pomeron, suggesting that the parton densities probed in inclusive diffractive ep interactions also increase rapidly at small x and that a single Pomeron trajectory cannot simultaneously describe the high- Q^2 diffractive data and the soft hadron-hadron data.

10.7 Comparison with models

As discussed earlier, the diffractive dissociation of virtual photons can be described in pQCD since the virtuality of the photon provides a hard scale. In the proton rest frame, the reaction can be viewed as the sequence of the photon fluctuating into a $q\bar{q}$ (or $q\bar{q}g$) colour dipole, the dipole scattering off the proton and producing the final state X. At high centre-of-mass energies, these processes are widely separated in time. The $q\bar{q}$, $q\bar{q}g$ fluctuations are described in terms of the photon wavefunction derived from QCD. The

interaction of the dipole with the proton is mediated, in the lowest order, by the exchange of two gluons in a colour-singlet state.

Several models of inclusive diffraction are available, which are discussed in review articles [2, 3]. The discussion of this section is restricted to two approaches based on the framework just outlined. The data were fitted (Section 10.7.1) with a parameterisation based on the model of Bartels et al. (BEKW) [48], which gives a satisfactory description of the earlier ZEUS results [7, 9]. It is interesting to see if the same parameterisation is able to describe the present data which cover a wider kinematic region; the fit is also a useful tool to compare the present data and those based on the ZEUS analysis using the M_X method [9].

In Section 10.7.2, the results of this paper are also compared with the Golec-Biernat and Wüsthoff model based on the idea of the saturation of the dipole-proton cross section [55], which successfully describes both the inclusive *ep* scattering data and earlier diffractive data.

Finally, Section 10.7.3 describes the results of an NLO QCD fit to the present high- Q^2 data. In this approach, the Q^2 dependence of the data is interpreted as due to the QCD evolution of the diffractive PDFs. A parameterisation of the diffractive PDFs at a starting scale is evolved according to the QCD evolution equations and fitted to the data.

10.7.1 BEKW fit

In the BEKW model [48], the dominant (leading-twist) contributions to the diffractive cross section in the kinematic domain of the present measurement come from fluctuations of transversely polarised virtual photons into either $q\bar{q}$ or $q\bar{q}g$ states. The β (and hence M_X) spectra of these two components are determined by general properties of the photon wave-function, with the $q\bar{q}$ contribution to the cross section proportional to $\beta(1-\beta)$ and the $q\bar{q}g$ contribution proportional to $(1-\beta)^{\gamma}$, where γ is a free parameter. For small values of M_X , the $q\bar{q}$ states dominate, while at large masses the $q\bar{q}g$ contribution becomes dominant. The model does not fix the $x_{\mathbb{P}}$ dependence of the $q\bar{q}$ and $q\bar{q}g$ contributions, but assumes for both a power-like behaviour, $x_{\mathbb{P}}^{-n(Q^2)}$, where the exponent n is determined from fits to the data. More explicitly, in the BEKW approach, the diffractive structure function can be parameterised as

$$x_{\mathbb{P}}F_2^{D(3)}(\beta, x_{\mathbb{P}}, Q^2) = c_T F_{q\bar{q}}^T + c_L F_{q\bar{q}}^L + c_g F_{q\bar{q}q}^T,$$

where

$$F_{q\bar{q}}^{T} = (x_0/x_{\mathbb{P}})^{n_T(Q^2)} \cdot \beta(1-\beta),$$

$$F_{q\bar{q}g}^{T} = (x_0/x_{\mathbb{P}})^{n_g(Q^2)} \cdot \ln(1+Q^2/Q_0^2) \cdot (1-\beta)^{\gamma}.$$

The contribution of longitudinal photons, $F_{q\bar{q}}^L$, which is relevant only at high β , was neglected in this analysis. A higher-twist term for $q\bar{q}$ states produced by transverse photons was also neglected. In the original BEKW model [48], the exponents $n_{T,g}(Q^2)$ are parameterised as $n_{T,g}(Q^2) = n_0^{T,g} + n_1^{T,g} \ln{(1 + \ln{Q^2}/Q_0^2)}$; here, this dependence was modified to $n_{T,g}(Q^2) = n_0^{T,g} + n_1^{T,g} \ln{(1 + Q^2/Q_0^2)}$, which is well defined also when $Q^2 \to 0$.

A fit was performed to the present high- Q^2 data using the parameterisation described above. The fit was limited to the region $x_{\mathbb{P}} < 0.01$, well within the diffractive peak. The parameters Q_0^2 , x_0 and $n_0^{T,g}$ were taken to be 0.4 GeV², 0.01, and 0.13, respectively ⁵. The coefficients c_T , c_g , $n_1^{T,g}$ and γ were determined in the fit, and have the following values: $c_T = 0.072 \pm 0.006 \text{(stat.)}, c_g = 0.008 \pm 0.001 \text{(stat.)}, n_1^{T,g} = 0.053 \pm 0.014 \text{(stat.)},$ $\gamma = 12.78 \pm 2.08 \text{(stat.)}$. The main features of the data are broadly reproduced by the fit, as shown in Fig. 7; the description of the Q^2 dependence of the diffractive to the inclusive cross-section ratio is also reasonable, as seen in Fig. 8. This indicates that the framework in which the incoming virtual photon fluctuates into a colour dipole is, in general, adequate to describe diffractive processes in ep collisions. At the same time, the data suggest the increasing importance of the contribution from $q\bar{q}g$ states at low Q^2 , as indicated in Fig. 7. The fit gives only a qualitative description of the low- Q^2 sample, which is outside the region of applicability of pQCD; these points were not included in the fit. The fit is also lower than the high- Q^2 data in the high- M_X bins that have $x_{\mathbb{P}} > 0.01$ -0.02, suggesting that different mechanisms, such as Reggeon exchange, are at work in the diffractive-peak region and at high $x_{\mathbb{P}}$. In this region the discrepancy between the data and the fit can be taken as an estimate of the contribution to the cross section due to exchanges other than the Pomeron.

10.7.2 Saturation model

In the saturation model by Golec-Biernat and Wüsthoff [55], diffractive DIS is also described in terms of the interaction of the $q\bar{q}$ ($q\bar{q}g$) fluctuation of the virtual photon with the proton. At high Q^2 , the dipole-proton cross section is obtained from pQCD and is proportional to the square of the transverse size of the dipole, which is in turn proportional to $1/Q^2$. As Q^2 decreases, the rise of the cross section with the dipole size would violate unitarity and is tamed by requiring that it saturates at a typical value of the hadron-hadron cross section. The value of Q^2 at which saturation occurs is x-dependent. The parameters of the model were obtained from a fit to F_2 data. The latest modification

⁵ Since $n_{T,g}(Q^2) = n_0^{T,g} + n_1^{T,g} \ln(1+Q^2/Q_0^2)$, n_0 gives the $x_{\mathbb{P}}$ dependence of $F_2^{D(3)}$ for $Q^2 \to 0$. If $F_2^{D(3)} \propto 1/x_{\mathbb{P}}^{2\bar{\alpha}_{\mathbb{P}}-1}$ is assumed and $\alpha_{\mathbb{P}}(t)$ is taken to be the soft Pomeron trajectory $(\alpha_{\mathbb{P}}(0) = 1.096, \alpha'_{\mathbb{P}} = 0.25 \text{ GeV}^{-2})$, then $n_0 = 0.13$.

of the model [51], denoted by BGK in the following, includes the QCD evolution of the gluon distribution.

Figures 11, 12 and 17 show the comparison of the measured structure function $F_2^{D(3)}$ with the BGK prediction [51]. In the region of applicability of the model, $x_{\mathbb{P}} \lesssim 0.01$ and Q^2 larger than a few GeV², the $x_{\mathbb{P}}$, Q^2 and β dependences of $F_2^{D(3)}$ are adequately described, although the data are slightly higher than the model prediction. The extrapolation of the model to large $x_{\mathbb{P}}$ values, beyond the Pomeron-dominated region, is significantly lower than the data, and the discrepancy increases with $x_{\mathbb{P}}$; in this region, the β dependences of the data and the model are also markedly different.

Both the BEKW and the saturation model imply Regge factorisation breaking. The fact that these models describe the data is not in contradiction with the possibility to fit the same data assuming Regge factorisation, as was done in Section 10.6, since the magnitude of the predicted violation is smaller than the precision of the present data.

10.7.3 QCD fit

An NLO QCD fit was performed to the present high- Q^2 data together with the recent ZEUS results on diffractive charm production in DIS [56]. The latter are important to constrain the gluon contribution to the diffractive PDFs. The fit was limited to the data in the region $Q^2 > 2$ GeV² and $x_{\mathbb{P}} < 0.01$. Regge factorisation was assumed, $F_2^{D(3)}(\beta, Q^2, x_{\mathbb{P}}) = f_{\mathbb{P}}(x_{\mathbb{P}}) \cdot F_2^{\mathbb{P}}(\beta, Q^2)$ (see Section 7), and the Pomeron flux was taken to be of the Donnachie-Landshoff form [53]

$$f_{\mathbb{P}}(x_{\mathbb{P}}, t) = \frac{9\beta_0^2}{4\pi^2 x_{\mathbb{P}}^{2\alpha_{\mathbb{P}}(t)-1}} [F_1(t)]^2,$$

where $\beta_0 = 1.8 \text{ GeV}^{-1}$, $F_1(t)$ is the elastic form factor of the proton, $\alpha_{\mathbb{P}}(0)$ was fixed to the result given in Section 10.6 and $\alpha'_{\mathbb{P}}$ was set to 0.25 GeV⁻². The results do not change if Eq. (9) is used.

The diffractive parton distributions (quark flavour singlet and gluon) were parameterised at the starting scale, $Q_0^2 = 2 \text{ GeV}^2$, using the general polynomial form $zf(z) = (a_1 + a_2z + a_3z^2) \cdot (1-z)^{a_4}$, where z is the parton fractional momentum. For the light quark distribution, it was assumed that $u = d = s = \bar{u} = \bar{d} = \bar{s}$; it was verified that setting the strange quark density to zero at the starting scale produces no appreciable change in the results. Charm quarks were treated in the Thorne-Roberts variable flavour number (TRVFN) scheme [57], with the charm-quark mass, m_c , set to 1.45 GeV. The NLO evolution package QCDNUM [58] was used to evolve the PDFs from the starting scale to the Q^2 values of each data point. The evolved PDFs were then fitted to the data.

The result of the fit is shown by the lines in Fig. 18. They satisfactorily reproduce the measurements, with $\chi^2/ndf = 37.8/36$ (statistical errors only). The resulting fraction of the t-channel momentum carried by gluons is $(82 \pm 8(\text{stat.})^{+5}_{-16}(\text{syst.}))\%$ at $Q^2 = 2 \text{ GeV}^2$, consistent with earlier ZEUS [59] and H1 [14] results, but higher than that found in a recent QCD analysis of the same data by Martin, Ryskin and Watt [60]. The systematic uncertainty includes the contributions listed in Section 9; in addition, the charm quark mass was varied between 1.3 and 1.6 GeV, and the relative normalisation between the charm and the $F_2^{D(3)}$ data was changed by $^{+11}_{-13}\%$, reflecting the uncertainty on the proton-dissociative background and on the luminosity in the charm data, as well as the normalisation uncertainty of the LPS data. The fixed-flavour-number scheme (FFNS) was used instead of TRVFN, without any significant change of the results. Various PDF parameterisations at the starting scale were tried, including the function used by H1 [14]. The shape of the fitted PDFs changes significantly depending on the functional form of the initial parameterisation, a consequence of the relatively large statistical uncertainties of the present sample. Therefore, these data cannot constrain the shapes of the PDFs. However, the integrals over z of the fitted PDFs and notably the fraction of the t-channel momentum carried by gluons are robust and change only slightly with the parameterisation chosen. This contribution was included in the systematic uncertainties quoted.

Also shown in Fig. 18 is the ratio of the charm contribution to the diffractive structure function, $F_2^{D(3),c\bar{c}}$ [56], and the present $F_2^{D(3)}$ results as a function of β (see Table 10). The ratio increases with increasing Q^2 and decreasing β , up to values of 30%. The ratio is well described by the fit.

11 Summary

New measurements have been presented of the reaction $e^+p \to e^+Xp$ in the regions $0.03 < Q^2 < 0.60 \text{ GeV}^2$ and $2 < Q^2 < 100 \text{ GeV}^2$. The scattered proton was measured in the ZEUS leading proton spectrometer, and was required to carry a fraction x_L of the incoming proton momentum of at least 90%. The data cover the region $0.075 < |t| < 0.35 \text{ GeV}^2$.

The results can be summarised as follows:

- the t dependence of the cross section is exponential, with a t-slope $b = 7.9 \pm 0.5 (\text{stat.})^{+0.8}_{-0.5} (\text{syst.})$ GeV⁻² for $x_{I\!\!P} < 0.01$. The slope is independent of Q^2 but decreases with $x_{I\!\!P}$;
- there is no observed Φ dependence of the cross section, indicating that the interference terms between the longitudinal and transverse amplitudes and between the two transverse amplitudes are consistent with zero in the measured kinematic region;

- the cross-section $d\sigma^{\gamma^*p\to Xp}/dM_X$ falls rapidly with Q^2 at high Q^2 but approaches a constant as $Q^2\to 0$. This behaviour is similar to that of the total photon-proton cross section, and is a consequence of the conservation of the electromagnetic current. In detail, it was found that the cross-section $d\sigma^{\gamma^*p\to Xp}/dM_X$ falls with Q^2 more slowly than $\sigma^{\gamma^*p}_{\text{tot}}$ when $Q^2 < M_X^2$ and faster than $\sigma^{\gamma^*p}_{\text{tot}}$ when $Q^2 > M_X^2$;
- the data were also analysed in terms of the structure function $F_2^{D(3)}$. The $x_{\mathbb{P}}$, Q^2 and β dependences of $F_2^{D(3)}$ were studied;
 - $F_2^{D(3)}$ falls with $x_{I\!\!P}$ faster than $1/x_{I\!\!P}$ for $x_{I\!\!P} \lesssim 0.01$ and more slowly at larger values of $x_{I\!\!P}$. From the $x_{I\!\!P}$ dependence of $F_2^{D(3)}$ at low $x_{I\!\!P}$, the Pomeron intercept $\alpha_{I\!\!P}(0)$ was measured to be $\alpha_{I\!\!P}(0) = 1.16 \pm 0.02$ (stat.) ± 0.02 (syst.), higher than that of the soft Pomeron, and similar to that measured in the photoproduction of heavy vector mesons. This suggests that, also in the present reaction, the virtual photon probes the proton in a region where the parton density increases quickly with decreasing x.
 - $F_2^{D(3)}$ rises with Q^2 over the whole measured region. The increase is very significant, about a factor five, between the low- Q^2 and the high- Q^2 region. In the high- Q^2 region, the rise becomes softer, and is reminiscent of the logarithmic scaling violations of the proton structure function. Positive scaling violations reflect a large gluon density. This is confirmed by an NLO QCD analysis of the present data for $x_{\mathbb{P}}$ < 0.01 in conjunction with the earlier ZEUS results on diffractive charm production [56]. The analysis indicates that the fraction of the t-channel momentum carried by gluons is $(82 \pm 8(\text{stat.})^{+5}_{-16}(\text{syst.}))\%$ at $Q^2 = 2 \text{ GeV}^2$. However, the present data are not precise enough to constrain the shapes of the PDFs.
 - The β dependence of $F_2^{D(3)}$ changes with $x_{\mathbb{IP}}$. For $x_{\mathbb{IP}} \lesssim 0.01$, $F_2^{D(3)}$ grows with β . For values of $x_{\mathbb{IP}} \gtrsim 0.01$ -0.02, $F_2^{D(3)}$ decreases with β . The latter behaviour is similar to that of the structure functions of hadrons as a function of x, and is consistent with the hypothesis that, at large $x_{\mathbb{IP}}$, the t-channel exchange mediating the photon-proton interaction is a meson-like object;
- the results presented are consistent, in the small $x_{\mathbb{P}}$ region, with the predictions of pQCD-based models of diffraction. In particular, the data were compared with models in which the virtual photon fluctuates into $q\bar{q}$ or $q\bar{q}g$ colour dipoles which then interact with the proton via the exchange of a gluon pair.

Acknowledgements

We thank the DESY Directorate for their support and encouragement. We are grateful for the support of the DESY computing and network services. We are specially grate-

ful to the HERA machine group: collaboration with them was crucial to the successful installation and operation of the leading proton spectrometer. The design, construction and installation of the ZEUS detector have been made possible by the ingenuity and effort of many people who are not listed as authors. It is also a pleasure to thank M. Diehl, K. Golec-Biernat, O. Nachtmann, N.N. Nikolaev, M.G. Ryskin and G. Watt for many useful discussions. We are grateful to K. Golec-Biernat for providing the prediction of his model for the kinematic range covered by our data.

References

- [1] P.D.B. Collins, An Introduction to Regge Theory and High Energy Physics, Cambridge University Press, Cambridge, 1977.
- [2] H. Abramowicz, Int. J. Mod. Phys. A 15 S1b, 495 (2000).
- [3] V. Barone and E. Predazzi, *High-Energy Particle Diffraction*, Springer Verlag, Heidelberg, 2002, and references therein.
- [4] L. Trentadue and G. Veneziano, Phys. Lett. **B 323**, 201 (1994).
- [5] J.C. Collins, Phys. Rev. **D** 57, 3051 (1998);Erratum, ibid. **D** 61, 019902 (2000).
- [6] A. Berera and D.E. Soper, Phys. Rev. **D** 53, 6162 (1996).
- [7] ZEUS Coll., S. Chekanov et al., Eur. Phys. J. C 25, 169 (2002).
- [8] ZEUS Coll., S. Chekanov et al., Nucl. Phys. B 658, 3 (2003).
- [9] ZEUS Coll., J. Breitweg et al., Eur. Phys. J. C 6, 43 (1999).
- [10] See e.g.: M. McDermott and G. Briskin, Proc. Workshop on Future Physics at HERA, G. Ingelman, A. De Roeck and R. Klanner (eds.), Vol. 2, p. 691. DESY, Hamburg, Germany (1996).
- [11] ZEUS Coll., J. Breitweg et al., Eur. Phys. J. C 1, 81 (1998).
- [12] ZEUS Coll., J. Breitweg et al., Eur. Phys. J. C 2, 237 (1998).
- [13] H1 Coll., C. Adloff et al., Nucl. Phys. **B 619**, 3 (2001).
- [14] H1 Coll., C. Adloff et al., Z. Phys. C 76, 613 (1997).
- [15] ZEUS Coll., U. Holm (ed.), *The ZEUS Detector*, Status Report (unpublished), DESY (1993), available on http://www-zeus.desy.de/bluebook/bluebook.html.
- [16] N. Harnew et al., Nucl. Inst. Meth. A 279, 290 (1989);
 B. Foster et al., Nucl. Phys. Proc. Suppl. B 32, 181 (1993);
 B. Foster et al., Nucl. Inst. Meth. A 338, 254 (1994).
- [17] M. Derrick et al., Nucl. Inst. Meth. A 309, 77 (1991);
 A. Andresen et al., Nucl. Inst. Meth. A 309, 101 (1991);
 A. Caldwell et al., Nucl. Inst. Meth. A 321, 356 (1992);
 A. Bernstein et al., Nucl. Inst. Meth. A 336, 23 (1993).
- [18] ZEUS Coll., J. Breitweg et al., Phys. Lett. B 407, 432 (1997).
- [19] ZEUS Coll., M. Derrick et al., Phys. Lett. B 487, 53 (2000).
- [20] A. Bamberger et al., Nucl. Inst. Meth. A 382, 419 (1996).

- [21] A. Dwuraźny et al., Nucl. Inst. Meth. A 277, 176 (1989).
- [22] ZEUS Coll., M. Derrick et al., Z. Phys. C 73, 253 (1997).
- [23] J. Andruszków et al., Technical Report DESY-92-066, DESY, 1992;
 ZEUS Coll., M. Derrick et al., Z. Phys. C 63, 391 (1994);
 J. Andruszków et al., Acta Phys. Pol. B 32, 2025 (2001).
- [24] H. Abramowicz, A. Caldwell and R. Sinkus, Nucl. Inst. Meth. A 365, 508 (1995).
- [25] S. Bentvelsen, J. Engelen and P. Kooijman, Proc. Workshop on Physics at HERA, W. Buchmüller and G. Ingelman (eds.), Vol. 1, p. 23. DESY, Hamburg, Germany (1992).
- [26] G. Briskin, Ph.D. Thesis, Tel Aviv University, DESY-THESIS-1998-036 (1988).
- [27] F. Jacquet and A. Blondel, Proc. Study of an ep Facility for Europe, U. Amaldi (ed.), p. 391. DESY, Hamburg, Germany (1979).
- [28] ZEUS Coll., S. Chekanov et al., Eur. Phys. J. C 21, 443 (2001).
- [29] M. Kasprzak, Ph.D. Thesis, University of Warsaw, DESY F35D-96-16 (1996).
- [30] M. Inuzuka, Ph.D. Thesis, University of Tokyo, KEK Report 99-9 (1999).
- [31] H. Jung, Comput. Phys. Commun. 86, 147 (1995).
- [32] G. Ingelmann and P.E. Schlein, Phys. Lett. B 152, 256 (1985).
- [33] J.F. Owens, Phys. Rev. **D** 30, 943 (1984).
- [34] B. List and A. Mastroberardino, Proc. Workshop on Monte Carlo Generators for HERA Physics, A.T. Doyle, G. Grindhammer, G. Ingelman and H. Jung (eds.), p. 396. DESY, Hamburg, Germany (1999). Also in preprint DESY-PROC-1999-02, available on http://www.desy.de/~heramc/.
- [35] K. Kwiatkowski, H. Spiesberger and H.-J. Möhring, Comput. Phys. Commun. 69, 155 (1992).
- [36] R. Brun et al., GEANT3, Technical Report CERN-DD/EE/84-1, CERN, 1987.
- [37] UA4 Coll., D. Bernard et al., Phys. Lett. B 186, 227 (1987).
- [38] M. Ruspa, Tesi di Dottorato, University of Torino, unpublished (2000).
- [39] B. Smalska, Ph.D. Thesis, University of Warsaw, unpublished (2001).
- [40] A. Mastroberardino, Tesi di Dottorato, University of Calabria, unpublished (2001).
- [41] N.N. Nikolaev, A.V. Pronyaev and B.G. Zakharov, JETP Lett. 68, 634 (1998).
- [42] A. Szczurek, N.N. Nikolaev and J. Speth, Phys. Lett. B 428, 383 (1998).
- [43] ZEUS Coll., J. Breitweg et al., Eur. Phys. J. C 12, 393 (2000).

- [44] T. Gehrmann and W.J. Stirling, Z. Phys. C 70, 89 (1996).
- [45] T. Arens et al., Z. Phys. C 74, 651 (1997).
- [46] M. Diehl, Z. Phys. C 76, 499 (1997).
- [47] N.N. Nikolaev, A.V. Pronyaev and B.G. Zakharov, Phys. Rev. **D** 59, 091501 (1999).
- [48] J. Bartels et al., Eur. Phys. J. C 7, 443 (1999).
- [49] H. Abramowicz and A. Levy, Preprint DESY-97-251 (hep-ph/9712415), DESY, 1997.
- [50] A. Levy, private communication (2004).
- [51] J. Bartels, K. Golec-Biernat and H. Kowalski, Phys. Rev. **D** 66, 014001 (2002).
- [52] J.-R. Cudell, K. Kang and S.K. Kim, Phys. Lett. **B** 395, 311 (1997).
- [53] A. Donnachie and P.V. Landshoff, Nucl. Phys. **B** 303, 634 (1988).
- [54] ZEUS Coll., S. Chekanov et al., Eur. Phys. J. C 24, 345 (2002).
- [55] K. Golec-Biernat and M. Wüsthoff, Phys. Rev. **D** 59, 014017 (1999);
 K. Golec-Biernat and M. Wüsthoff, Phys. Rev. **D** 60, 114023 (1999);
 K. Golec-Biernat and M. Wüsthoff, Eur. Phys. J. C 20, 313 (2001).
- [56] ZEUS Coll., S. Chekanov et al., Nucl. Phys. B 672, 3 (2003).
- [57] R.S. Thorne, J. Phys. G 25, 1307 (1999);
 R.S. Thorne and R.G. Roberts, Phys. Lett. B 421, 303 (1998);
 R.S. Thorne and R.G. Roberts, Phys. Rev. D 57, 6871 (1998);
 R.S. Thorne and R.G. Roberts, Eur. Phys. J. C 19, 339 (2001).
- [58] M.A.J. Botje, Computer code QCDNUM version 16.12, National Institute for Nuclear and High Energy Physics, Amsterdam, The Netherlands, 1998 (unpublished).
- [59] ZEUS Coll., S. Breitweg et al., Eur. Phys. J. C 5, 41 (1998).
- [60] A.D. Martin, M.G. Ryskin and G. Watt, Preprint IPPP/04/09 and DCPT/04/18 (hep-ph/0406224), University of Duhram, 2004.

$\langle Q^2 \rangle \; (\text{GeV}^2)$	$\langle \beta \rangle$	$\langle x_{I\!\!P} \rangle$	$b \; (\mathrm{GeV^{-2}})$
7.1	0.37	0.001	$8.13 \pm 0.68^{+0.95}_{-0.53}$
10.2	0.24	0.006	$7.87 \pm 0.83^{+1.21}_{-0.66}$
11.5	0.14	0.019	$6.14 \pm 0.82^{+1.73}_{-0.68}$
11.7	0.07	0.04	$4.19 \pm 0.62^{+0.83}_{-0.75}$
12.2	0.05	0.06	$4.19 \pm 0.40^{+0.42}_{-0.30}$

 $\textbf{Table 1:} \quad \textit{Fitted values of the t-slopes.} \quad \textit{The first uncertainty is statistical, the second systematic.}$

$\langle Q^2 \rangle \; (\mathrm{GeV^2})$	$\langle \beta \rangle$	$\langle x_{I\!\!P} \rangle$	$\langle t \rangle \; (\text{GeV}^2)$	A_{LT}
13.0	0.48	0.0009	0.145	$-0.06 \pm 0.13^{+0.12}_{-0.08}$
17.7	0.34	0.0029	0.145	$0.06 \pm 0.16^{+0.04}_{-0.17}$
20.3	0.27	0.0068	0.145	$-0.02 \pm 0.15^{+0.09}_{-0.04}$
21.1	0.18	0.0190	0.147	$0.02 \pm 0.11^{+0.09}_{-0.04}$
22.5	0.11	0.041	0.151	$-0.15 \pm 0.13^{+0.05}_{-0.22}$
23.0	0.08	0.061	0.161	$0.10 \pm 0.08^{+0.10}_{-0.04}$
9.6	0.04	0.0064	0.145	$-0.05 \pm 0.29^{+0.15}_{-0.16}$
14.4	0.13	0.0042	0.145	$-0.19 \pm 0.19^{+0.15}_{-0.23}$
17.7	0.38	0.0030	0.145	$0.03 \pm 0.12^{+0.08}_{-0.05}$
20.1	0.73	0.0024	0.145	$0.14 \pm 0.19^{+0.18}_{-0.08}$
17.0	0.37	0.0035	0.085	$0.03 \pm 0.16^{+0.07}_{-0.09}$
17.0	0.37	0.0035	0.11	$0.00 \pm 0.17^{+0.11}_{-0.09}$
17.0	0.37	0.0035	0.15	$0.02 \pm 0.18^{+0.09}_{-0.07}$
17.0	0.37	0.0035	0.24	$-0.14 \pm 0.17^{+0.15}_{-0.05}$
7.8	0.28	0.0025	0.145	$0.01 \pm 0.16^{+0.08}_{-0.13}$
11.8	0.37	0.0033	0.145	$-0.13 \pm 0.15^{+0.07}_{-0.08}$
16.9	0.42	0.0039	0.145	$0.01 \pm 0.18^{+0.16}_{-0.02}$
36.0	0.44	0.0046	0.145	$0.10 \pm 0.19^{+0.07}_{-0.11}$

Table 2: Fitted values of the asymmetry parameter A_{LT} . The first uncertainty is statistical, the second systematic.

$\langle Q^2 \rangle \; (\mathrm{GeV^2})$	$\langle M_X \rangle$ (GeV)	$\langle W \rangle \text{ (GeV)}$	$d\sigma^{\gamma^*p\to Xp}/dM_X \; (\mu \mathrm{b/GeV})$
0.33	5	100	$0.469 \pm 0.095^{+0.037}_{-0.031}$
0.29	5	160	$0.355 {\pm} 0.075^{+0.035}_{-0.021}$
0.24	5	190	$0.60 \pm 0.14 ^{+0.07}_{-0.04}$
0.14	5	245	$0.61 \pm 0.22 ^{+0.05}_{-0.04}$
0.34	22	100	$0.113 \pm 0.020^{+0.009}_{-0.010}$
0.34	22	160	$0.115 \pm 0.029^{+0.011}_{-0.007}$
0.27	22	190	$0.095 \pm 0.041^{+0.009}_{-0.004}$
0.33	40	160	$0.046 \pm 0.010^{+0.003}_{-0.004}$
0.24	40	190	$0.055 \pm 0.012^{+0.004}_{-0.005}$
0.13	40	245	$0.081 \pm 0.021^{+0.006}_{-0.005}$
0.09	40	275	$0.218 \pm 0.059^{+0.025}_{-0.030}$

Table 3: The diffractive cross section, $d\sigma^{\gamma^*p\to Xp}/dM_X$, for the low- Q^2 sample. The first uncertainty given is statistical, the second systematic.

$Q^2 (\text{GeV}^2)$	M_X (GeV)	W (GeV)	$d\sigma^{\gamma^* p \to Xp}/dM_X \; (\mu b/\text{GeV})$
2.7	5	100	$0.179 \pm 0.022^{+0.030}_{-0.006}$
4.5	5	100	$0.119 \pm 0.013^{+0.013}_{-0.008}$
10.0	5	100	$0.074 \pm 0.006^{+0.009}_{-0.005}$
35.0	5	100	$0.015 \pm 0.002^{+0.002}_{-0.001}$
2.7	22	100	$0.082 \pm 0.006^{+0.010}_{-0.004}$
4.5	22	100	$0.052 \pm 0.004^{+0.007}_{-0.004}$
10.0	22	100	$0.025 \pm 0.001^{+0.003}_{-0.001}$
35.0	22	100	$0.009 \pm 0.001^{+0.001}_{-0.001}$
2.7	5	160	$0.230 \pm 0.027^{+0.021}_{-0.019}$
4.5	5	160	$0.178 \pm 0.028^{+0.011}_{-0.011}$
10.0	5	160	$0.082 \pm 0.008^{+0.007}_{-0.005}$
35.0	5	160	$0.015 \pm 0.002^{+0.002}_{-0.001}$
2.7	22	160	$0.048 \pm 0.006^{+0.007}_{-0.002}$
4.5	22	160	$0.033 \pm 0.005^{+0.003}_{-0.004}$
10.0	22	160	$0.016 \pm 0.002^{+0.002}_{-0.001}$
35.0	22	160	$0.007 \pm 0.001^{+0.001}_{-0.001}$
2.7	40	160	$0.051 \pm 0.007^{+0.010}_{-0.007}$
4.5	40	160	$0.037 \pm 0.004^{+0.005}_{-0.002}$
10.0	40	160	$0.020 \pm 0.002^{+0.003}_{-0.001}$
35.0	40	160	$0.006 \pm 0.001^{+0.001}_{-0.000}$
2.7	5	190	$0.240 \pm 0.035^{+0.021}_{-0.026}$
4.5	5	190	$0.163 \pm 0.024^{+0.016}_{-0.012}$
10.0	5	190	$0.098 \pm 0.012^{+0.009}_{-0.016}$
35.0	5	190	$0.021 \pm 0.004^{+0.002}_{-0.003}$
2.7	22	190	$0.064 \pm 0.012^{+0.007}_{-0.008}$
4.5	22	190	$0.041 \pm 0.009^{+0.005}_{-0.004}$
10.0	22	190	$0.019 \pm 0.003^{+0.002}_{-0.002}$
35.0	22	190	$0.009 \pm 0.002^{+0.001}_{-0.001}$
2.7	40	190	$0.046 \pm 0.006^{+0.005}_{-0.004}$
4.5	40	190	$0.040 \pm 0.005^{+0.004}_{-0.004}$
10.0	40	190	$0.019 \pm 0.002^{+0.003}_{-0.001}$
35.0	40	190	$0.007 \pm 0.001^{+0.001}_{-0.001}$

Table 4: The diffractive cross section, $d\sigma^{\gamma^*p\to Xp}/dM_X$, for the high- Q^2 sample. The first uncertainty given is statistical, the second systematic.

$\langle Q^2 \rangle \; (\mathrm{GeV^2})$	$\langle \beta \rangle$	$\langle x_{I\!\!P} \rangle$	$x_{I\!\!P} F_2^{D(3)}$
0.10	0.0002	0.023	$0.00122 \pm 0.00045^{+0.00015}_{-0.00007}$
0.14	0.0002	0.066	$0.00307 \pm 0.00044^{+0.00022}_{-0.00037}$
0.12	0.0006	0.011	$0.00156 \pm 0.00062^{+0.00016}_{-0.00011}$
0.15	0.0006	0.050	$0.00376 \pm 0.00055^{+0.00028}_{-0.00036}$
0.12	0.0019	0.0033	$0.0024 \pm 0.0010 ^{+0.0003}_{-0.0001}$
0.15	0.0019	0.0077	$0.00239 \pm 0.00092^{+0.00027}_{-0.00011}$
0.16	0.0019	0.022	$0.0034 \pm 0.0014 ^{+0.0004}_{-0.0005}$
0.12	0.008	0.0010	$0.00246 \pm 0.00079^{+0.00026}_{-0.00034}$
0.15	0.007	0.0027	$0.00177 \pm 0.00075^{+0.00017}_{-0.00020}$
0.16	0.007	0.0057	$0.0031 \pm 0.0014 ^{+0.0003}_{-0.0002}$
0.19	0.006	0.018	$0.0036 \pm 0.0019 ^{+0.0004}_{-0.0003}$
0.17	0.03	0.00021	$0.0036 \pm 0.0012 ^{+0.0004}_{-0.0002}$
0.20	0.03	0.00046	$0.00262 \pm 0.00094^{+0.00025}_{-0.00012}$
0.21	0.03	0.0011	$0.0032 \pm 0.0011 ^{+0.0002}_{-0.0003}$
0.22	0.03	0.0031	$0.0032 \pm 0.0015 ^{+0.0003}_{-0.0002}$

Table 5: The diffractive structure function multiplied by $x_{\mathbb{I\!P}}$, $x_{\mathbb{I\!P}}F_2^{D(3)}(\beta, Q^2, x_{\mathbb{I\!P}})$, for the low- Q^2 sample. The first uncertainty given is statistical, the second systematic.

$\langle Q^2 \rangle \; (\mathrm{GeV^2})$	$\langle \beta \rangle$	$\langle x_{I\!\!P} \rangle$	$x_{I\!\!P}F_2^{D(3)}$
0.13	0.0077	0.0012	$0.00257 \pm 0.00071^{+0.00029}_{-0.00028}$
0.16	0.023	0.0012	$0.00284 \pm 0.00077^{+0.00025}_{-0.00017}$
0.11	0.0016	0.0028	$0.00162 \pm 0.00065^{+0.00011}_{-0.00018}$
0.19	0.022	0.0028	$0.0029 \pm 0.0010 ^{+0.0002}_{-0.0002}$
0.13	0.0012	0.0068	$0.00214 \pm 0.00069^{+0.00031}_{-0.00010}$
0.16	0.0073	0.0068	$0.00197 \pm 0.00067^{+0.00019}_{-0.00013}$
0.10	0.00024	0.019	$0.0032 \pm 0.0010 ^{+0.0005}_{-0.0002}$
0.15	0.0015	0.019	$0.0043 \pm 0.0013 ^{+0.0003}_{-0.0005}$
0.10	0.000062	0.067	$0.00094 \pm 0.00018^{+0.00007}_{-0.00005}$
0.14	0.00019	0.066	$0.00307 \pm 0.00044^{+0.00022}_{-0.00037}$

Table 6: The diffractive structure function multiplied by $x_{\mathbb{IP}}$, $x_{\mathbb{IP}}F_2^{D(3)}(\beta, Q^2, x_{\mathbb{IP}})$, for the low- Q^2 sample. The first uncertainty given is statistical, the second systematic. These are the points plotted in Fig. 12. The data in this table are not independent of those in Table 5.

$Q^2 (\text{GeV}^2)$	β	$x_{I\!\!P}$	$x_{I\!\!P} F_2^{D(3)}$
2.4	0.0070	0.0068	$0.0117 \pm 0.0041^{+0.0101}_{-0.0006}$
2.4	0.0070	0.0190	$0.0146 \pm 0.0023^{+0.0039}_{-0.0000}$
2.4	0.0070	0.0400	$0.0166 \pm 0.0032^{+0.0021}_{-0.0014}$
2.4	0.0070	0.0600	$0.0212 \pm 0.0023^{+0.0023}_{-0.0025}$
2.4	0.0300	0.0028	$0.0141 \pm 0.0038^{+0.0025}_{-0.0022}$
2.4	0.0300	0.0068	$0.0139 \pm 0.0035^{+0.0038}_{-0.0003}$
2.4	0.0300	0.0190	$0.0123 \pm 0.0025^{+0.0038}_{-0.0002}$
2.4	0.0300	0.0400	$0.0150 \pm 0.0023^{+0.0047}_{-0.0040}$
2.4	0.0300	0.0600	$0.0218 \pm 0.0031^{+0.0030}_{-0.0019}$
2.4	0.1300	0.0005	$0.0163 \pm 0.0033^{+0.0000}_{-0.0089}$
2.4	0.1300	0.0012	$0.0184 \pm 0.0035^{+0.0011}_{-0.0034}$
2.4	0.1300	0.0028	$0.0131 \pm 0.0028^{+0.0029}_{-0.0033}$
2.4	0.1300	0.0068	$0.0164 \pm 0.0035^{+0.0013}_{-0.0071}$
2.4	0.1300	0.0190	$0.0173 \pm 0.0033^{+0.0019}_{-0.0007}$
2.4	0.4800	0.0005	$0.0331 \pm 0.0056^{+0.0019}_{-0.0039}$
2.4	0.4800	0.0012	$0.0271 \pm 0.0054^{+0.0097}_{-0.0030}$
2.4	0.4800	0.0028	$0.0181 \pm 0.0040^{+0.0052}_{-0.0051}$
3.7	0.0070	0.0190	$0.0134 \pm 0.0022^{+0.0017}_{-0.0011}$
3.7	0.0070	0.0400	$0.0183 \pm 0.0027^{+0.0037}_{-0.0014}$
3.7	0.0070	0.0600	$0.0282 \pm 0.0039^{+0.0046}_{-0.0017}$
3.7	0.0300	0.0028	$0.0206 \pm 0.0058^{+0.0008}_{-0.0081}$
3.7	0.0300	0.0068	$0.0191 \pm 0.0046^{+0.0050}_{-0.0007}$
3.7	0.0300	0.0190	$0.0102 \pm 0.0032^{+0.0051}_{-0.0001}$
3.7	0.0300	0.0400	$0.0134 \pm 0.0022^{+0.0031}_{-0.0005}$
3.7	0.0300	0.0600	$0.0211 \pm 0.0022^{+0.0031}_{-0.0018}$

Table 7: The diffractive structure function multiplied by $x_{\mathbb{P}}$, $x_{\mathbb{P}}F_2^{D(3)}(\beta, Q^2, x_{\mathbb{P}})$, for the high- Q^2 sample, part I. The first uncertainty given is statistical, the second systematic.

$Q^2 (\text{GeV}^2)$	β	$x_{I\!\!P}$	$x_{I\!\!P} F_2^{D(3)}$
3.7	0.1300	0.0005	$0.0243\pm0.0060^{+0.0064}_{-0.0012}$
3.7	0.1300	0.0012	$0.0194 \pm 0.0037^{+0.0029}_{-0.0024}$
3.7	0.1300	0.0028	$0.0142 \pm 0.0027^{+0.0022}_{-0.0019}$
3.7	0.1300	0.0068	$0.0087 \pm 0.0019^{+0.0030}_{-0.0000}$
3.7	0.1300	0.0190	$0.0106 \pm 0.0016^{+0.0009}_{-0.0016}$
3.7	0.1300	0.0400	$0.0089 \pm 0.0019^{+0.0007}_{-0.0018}$
3.7	0.4800	0.0005	$0.0423 \pm 0.0056^{+0.0045}_{-0.0024}$
3.7	0.4800	0.0012	$0.0355 \pm 0.0058^{+0.0064}_{-0.0033}$
3.7	0.4800	0.0028	$0.0277 \pm 0.0062^{+0.0074}_{-0.0008}$
3.7	0.4800	0.0068	$0.0234 \pm 0.0046^{+0.0034}_{-0.0055}$
6.9	0.0070	0.0190	$0.0182 \pm 0.0031^{+0.0043}_{-0.0027}$
6.9	0.0070	0.0400	$0.0250 \pm 0.0030^{+0.0040}_{-0.0013}$
6.9	0.0070	0.0600	$0.0274 \pm 0.0024^{+0.0033}_{-0.0019}$
6.9	0.0300	0.0068	$0.0206 \pm 0.0038^{+0.0065}_{-0.0017}$
6.9	0.0300	0.0190	$0.0138 \pm 0.0017^{+0.0020}_{-0.0003}$
6.9	0.0300	0.0400	$0.0139 \pm 0.0031^{+0.0020}_{-0.0025}$
6.9	0.0300	0.0600	$0.0281 \pm 0.0032^{+0.0057}_{-0.0013}$
6.9	0.1300	0.0012	$0.0237 \pm 0.0044^{+0.0058}_{-0.0025}$
6.9	0.1300	0.0028	$0.0196 \pm 0.0032^{+0.0010}_{-0.0051}$
6.9	0.1300	0.0068	$0.0114 \pm 0.0020^{+0.0016}_{-0.0014}$
6.9	0.1300	0.0190	$0.0136 \pm 0.0018^{+0.0031}_{-0.0011}$
6.9	0.1300	0.0400	$0.0147 \pm 0.0026^{+0.0025}_{-0.0006}$
6.9	0.1300	0.0600	$0.0190 \pm 0.0033^{+0.0031}_{-0.0012}$
6.9	0.4800	0.0005	$0.0436 \pm 0.0053^{+0.0060}_{-0.0026}$
6.9	0.4800	0.0012	$0.0333 \pm 0.0043^{+0.0037}_{-0.0013}$
6.9	0.4800	0.0028	$0.0275 \pm 0.0042^{+0.0044}_{-0.0014}$
6.9	0.4800	0.0068	$0.0260 \pm 0.0041^{+0.0042}_{-0.0024}$
6.9	0.4800	0.0190	$0.0156 \pm 0.0028^{+0.0017}_{-0.0024}$

Table 8: The diffractive structure function multiplied by $x_{\mathbb{P}}$, $x_{\mathbb{P}}F_2^{D(3)}(\beta, Q^2, x_{\mathbb{P}})$, for the high- Q^2 sample, part II. The first uncertainty given is statistical, the second systematic.

$Q^2 (\text{GeV}^2)$	β	$x_{I\!\!P}$	$x_{I\!\!P} F_2^{D(3)}$
13.5	0.0070	0.0400	$0.0406 \pm 0.0073^{+0.0126}_{-0.0036}$
13.5	0.0070	0.0600	$0.0420 \pm 0.0046^{+0.0061}_{-0.0028}$
13.5	0.0300	0.0190	$0.0207 \pm 0.0039^{+0.0025}_{-0.0014}$
13.5	0.0300	0.0400	$0.0264 \pm 0.0037^{+0.0074}_{-0.0032}$
13.5	0.0300	0.0600	$0.0303 \pm 0.0032^{+0.0041}_{-0.0030}$
13.5	0.1300	0.0028	$0.0210 \pm 0.0046^{+0.0043}_{-0.0033}$
13.5	0.1300	0.0068	$0.0165 \pm 0.0028^{+0.0032}_{-0.0010}$
13.5	0.1300	0.0190	$0.0157 \pm 0.0021^{+0.0026}_{-0.0008}$
13.5	0.1300	0.0400	$0.0175 \pm 0.0027^{+0.0010}_{-0.0050}$
13.5	0.1300	0.0600	$0.0210 \pm 0.0027^{+0.0030}_{-0.0032}$
13.5	0.4800	0.0005	$0.0483 \pm 0.0108^{+0.0185}_{-0.0011}$
13.5	0.4800	0.0012	$0.0326 \pm 0.0046^{+0.0032}_{-0.0023}$
13.5	0.4800	0.0028	$0.0262 \pm 0.0040^{+0.0017}_{-0.0068}$
13.5	0.4800	0.0068	$0.0202 \pm 0.0031^{+0.0034}_{-0.0009}$
13.5	0.4800	0.0190	$0.0236 \pm 0.0041^{+0.0040}_{-0.0026}$
13.5	0.4800	0.0400	$0.0140\pm0.0030^{+0.0056}_{-0.0002}$
39.0	0.0300	0.0400	$0.0379 \pm 0.0066^{+0.0063}_{-0.0038}$
39.0	0.0300	0.0600	$0.0394 \pm 0.0045^{+0.0057}_{-0.0037}$
39.0	0.1300	0.0068	$0.0303 \pm 0.0070^{+0.0007}_{-0.0122}$
39.0	0.1300	0.0190	$0.0223 \pm 0.0033^{+0.0063}_{-0.0005}$
39.0	0.1300	0.0400	$0.0203 \pm 0.0033^{+0.0031}_{-0.0023}$
39.0	0.1300	0.0600	$0.0289 \pm 0.0033^{+0.0041}_{-0.0033}$
39.0	0.4800	0.0028	$0.0287 \pm 0.0056^{+0.0040}_{-0.0032}$
39.0	0.4800	0.0068	$0.0212 \pm 0.0041^{+0.0028}_{-0.0019}$
39.0	0.4800	0.0190	$0.0176 \pm 0.0029^{+0.0033}_{-0.0012}$
39.0	0.4800	0.0400	$0.0200 \pm 0.0042^{+0.0052}_{-0.0017}$
39.0	0.4800	0.0600	$0.0190 \pm 0.0033^{+0.0033}_{-0.0041}$

Table 9: The diffractive structure function multiplied by $x_{\mathbb{P}}$, $x_{\mathbb{P}}F_2^{D(3)}(\beta, Q^2, x_{\mathbb{P}})$, for the high- Q^2 sample, part III. The first uncertainty given is statistical, the second systematic.

$Q^2 (\mathrm{GeV}^2)$	β	$x_{I\!\!P}$	$F_2^{D(3),c\bar{c}}/F_2^{D(3)}$
4.0	0.02	0.004	$0.29 \pm 0.12^{+0.10}_{-0.16}$
4.0	0.05	0.004	$0.20 \pm 0.08^{+0.06}_{-0.05}$
4.0	0.2	0.004	$0.06 \pm 0.02^{+0.02}_{-0.02}$
25.0	0.2	0.004	$0.35 \pm 0.10^{+0.09}_{-0.06}$
25.0	0.5	0.004	$0.15 \pm 0.05^{+0.04}_{-0.03}$

Table 10: The ratio of $F_2^{D(3),c\bar{c}}$ [56] and the present $F_2^{D(3)}$ measurement. The first uncertainty given is statistical, the second systematic.

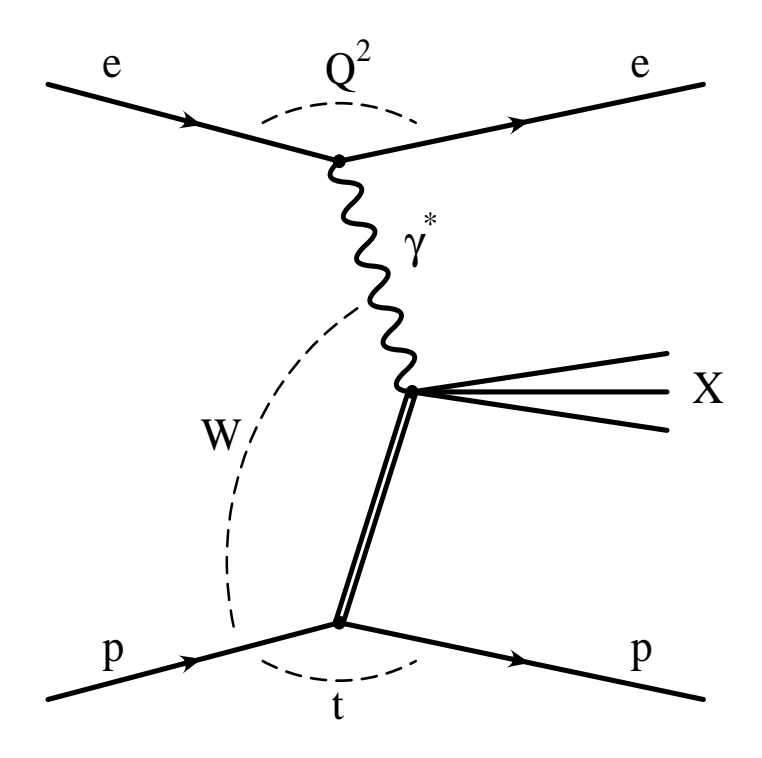


Figure 1: Schematic diagram of the reaction $ep \rightarrow eXp$.

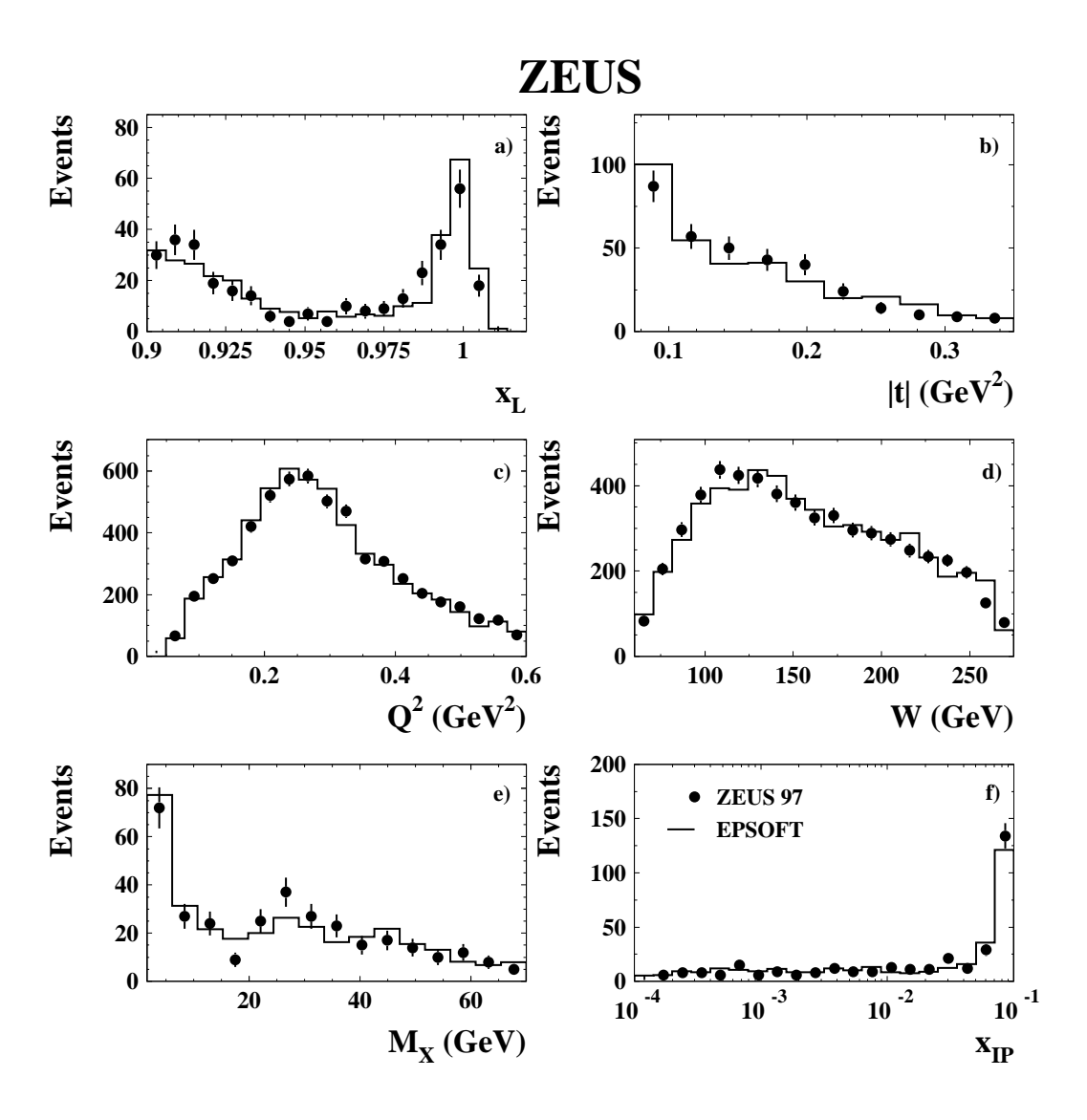


Figure 2: Comparison of the measured (points) and Monte-Carlo simulated (histograms) distributions for x_L , |t|, Q^2 , W, M_X and $x_{\mathbb{P}}$ in the low- Q^2 analysis. The Q^2 and W distributions were obtained without the LPS requirement (see text).

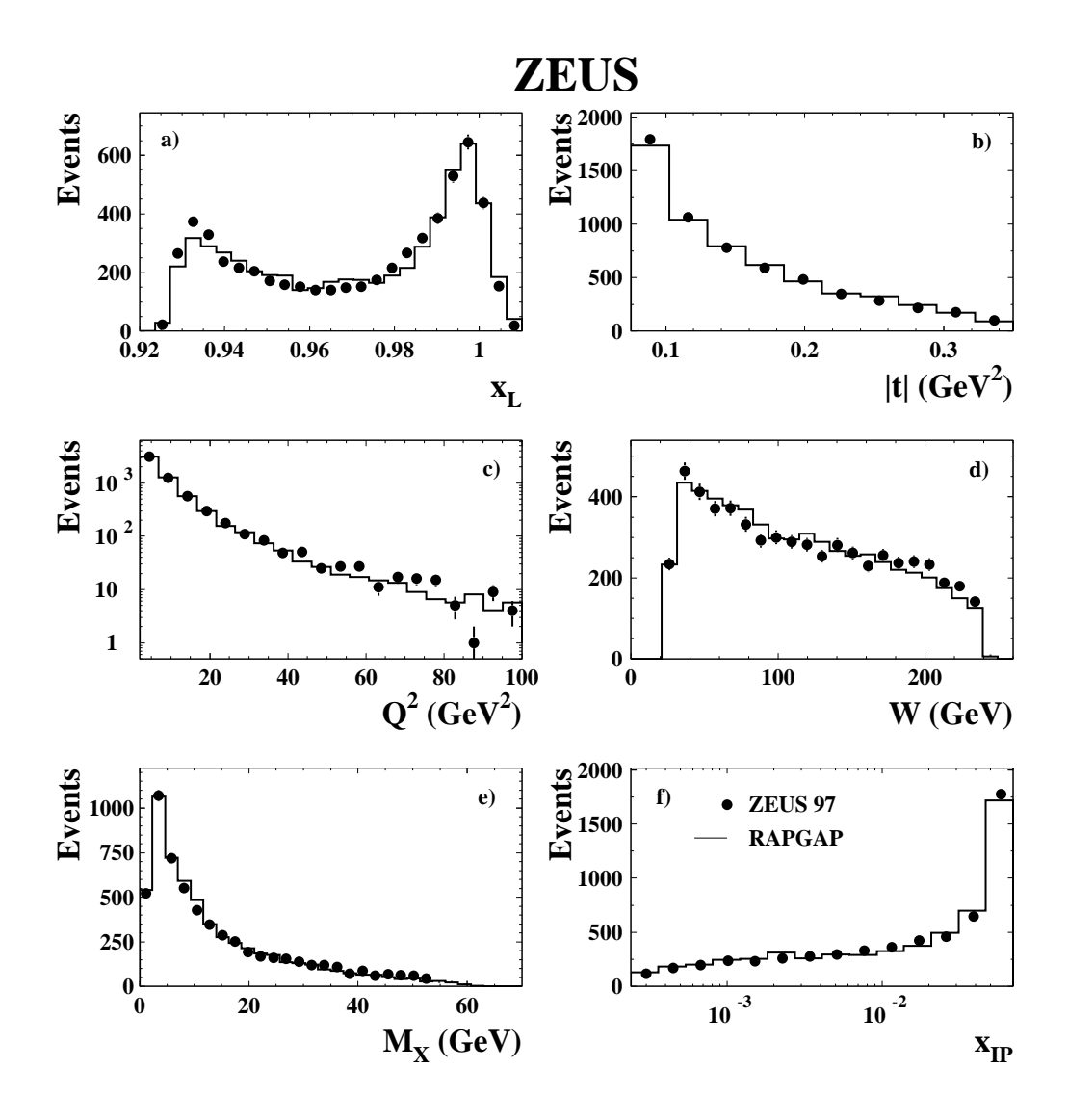


Figure 3: Comparison of the measured (points) and Monte-Carlo simulated (histograms) distributions for x_L , |t|, Q^2 , W, M_X and $x_{\mathbb{P}}$ in the high- Q^2 analysis.

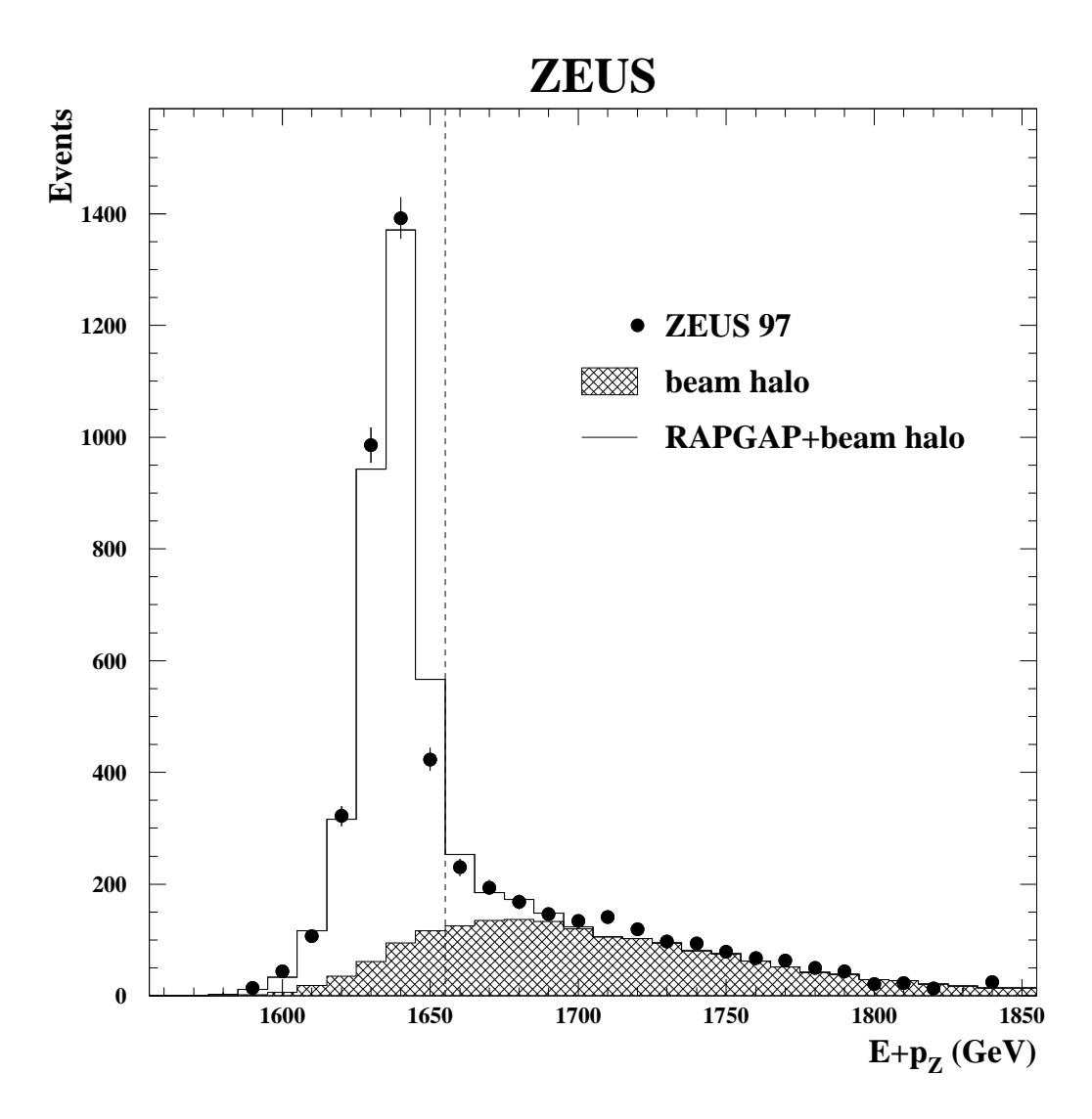


Figure 4: Distribution of $E+p_Z$ for the high- Q^2 events. The hatched histogram represents the beam-halo sample obtained as discussed in the text. The empty histogram is the sum of the RAPGAP Monte Carlo and the beam-halo contribution. The vertical dashed line is at $E+p_Z=1655~{\rm GeV}$, the value of the cut used to suppress beam-halo events.

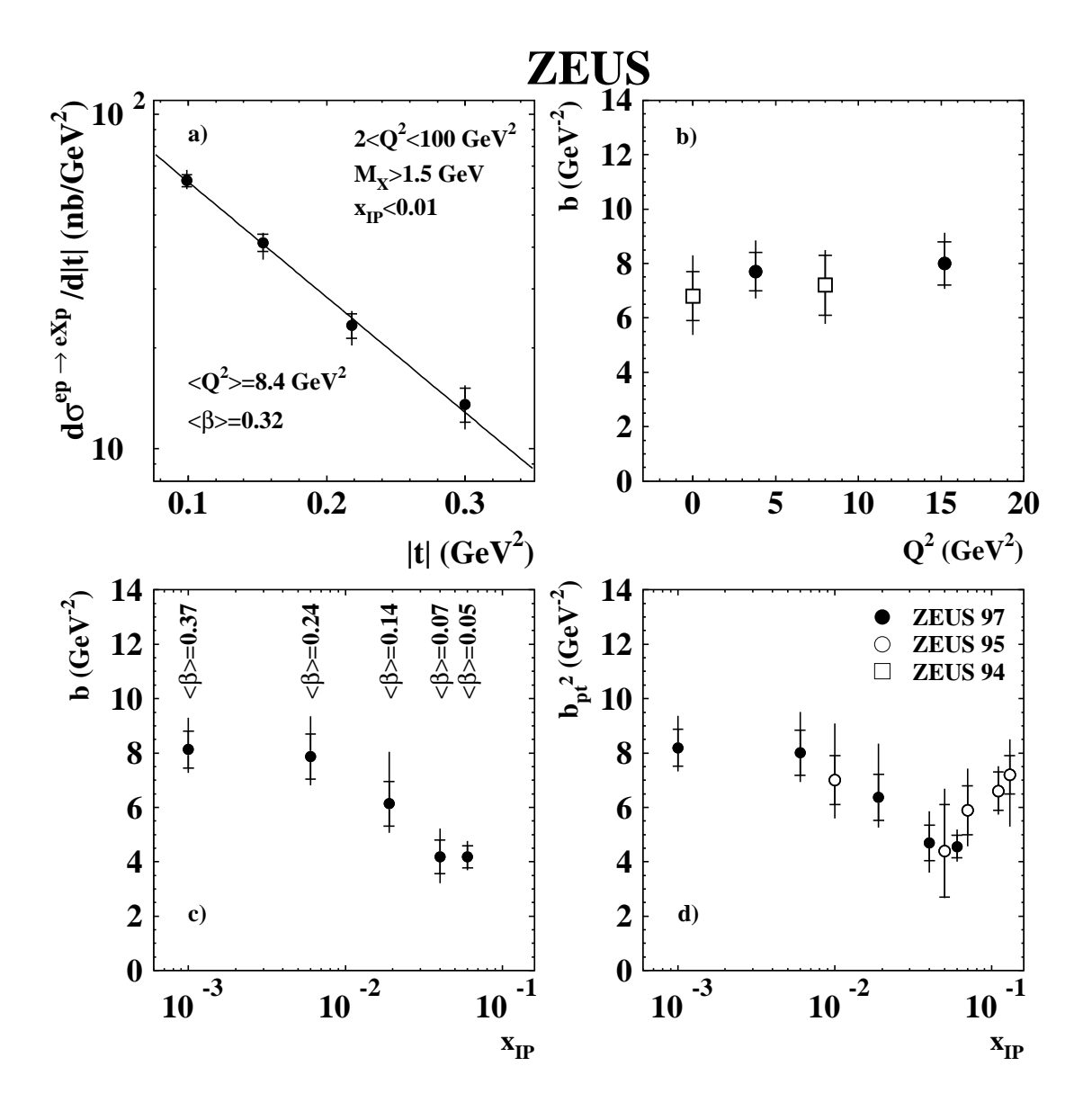


Figure 5: (a) The differential cross-section $d\sigma^{ep\to eXp}/dt$ in the region $x_{\mathbb{P}} < 0.01$, $2 < Q^2 < 100 \text{ GeV}^2$ and $M_X > 1.5 \text{ GeV}$. The inner error bars show the statistical uncertainties and the full bars indicate the statistical and the systematic uncertainties added in quadrature. The overall normalisation uncertainty of $\pm 10\%$ is not shown. The line shows the result of the fit described in the text. (b) The value of the slope parameter b of the differential cross-section $d\sigma^{ep\to eXp}/dt$ as a function of Q^2 . (c) The value of the slope parameter b of the differential cross-section $d\sigma^{ep\to eXp}/dt$ as a function of $x_{\mathbb{P}}$. The mean value of β in each bin is also given. (d) The value of the slope parameter $b_{p_T^2}$ of the differential cross-section $d\sigma^{ep\to eXp}/dp_T^2$ as a function of $x_{\mathbb{P}}$. The symbols labelled ZEUS 97 indicate the present results. Earlier ZEUS results are also shown: ZEUS 95 [8], ZEUS 94 [12] $(Q^2 = 0)$ and ZEUS 94 [11] $(Q^2 > 0)$.

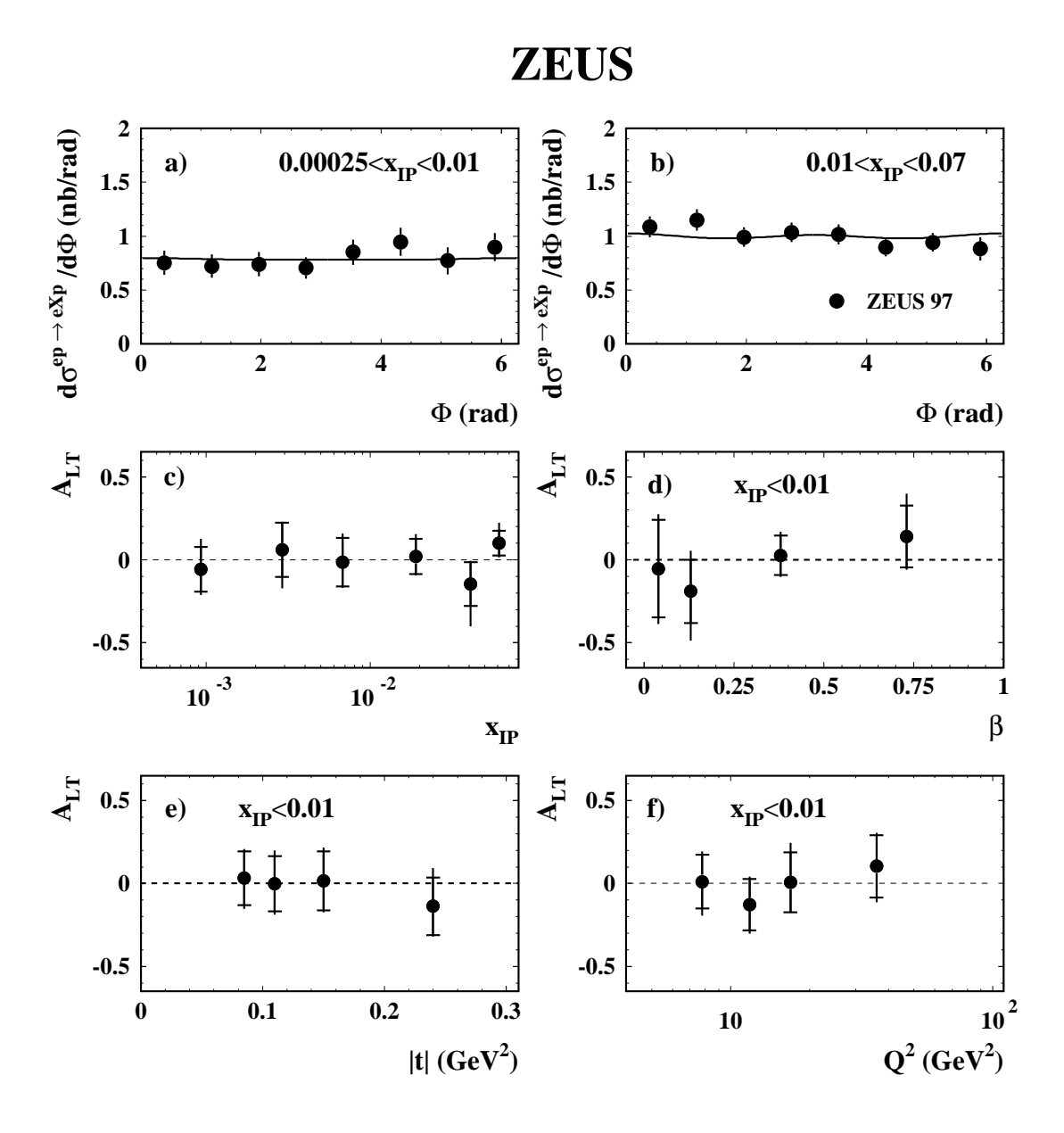


Figure 6: The differential cross-section $d\sigma^{ep\to eXp}/d\Phi$ in the kinematic ranges (a) $0.00025 < x_{\mathbb{IP}} < 0.01$ and (b) $0.01 < x_{\mathbb{IP}} < 0.07$. The error bars show the statistical uncertainty. The line shows the result of the fit described in the text. The azimuthal asymmetry A_{LT} as a function of (c) $x_{\mathbb{IP}}$, (d) β , (e) |t| and (f) Q^2 for $x_{\mathbb{IP}} < 0.01$. The inner error bars show the statistical uncertainties and the full bars indicate the statistical and the systematic uncertainties added in quadrature.

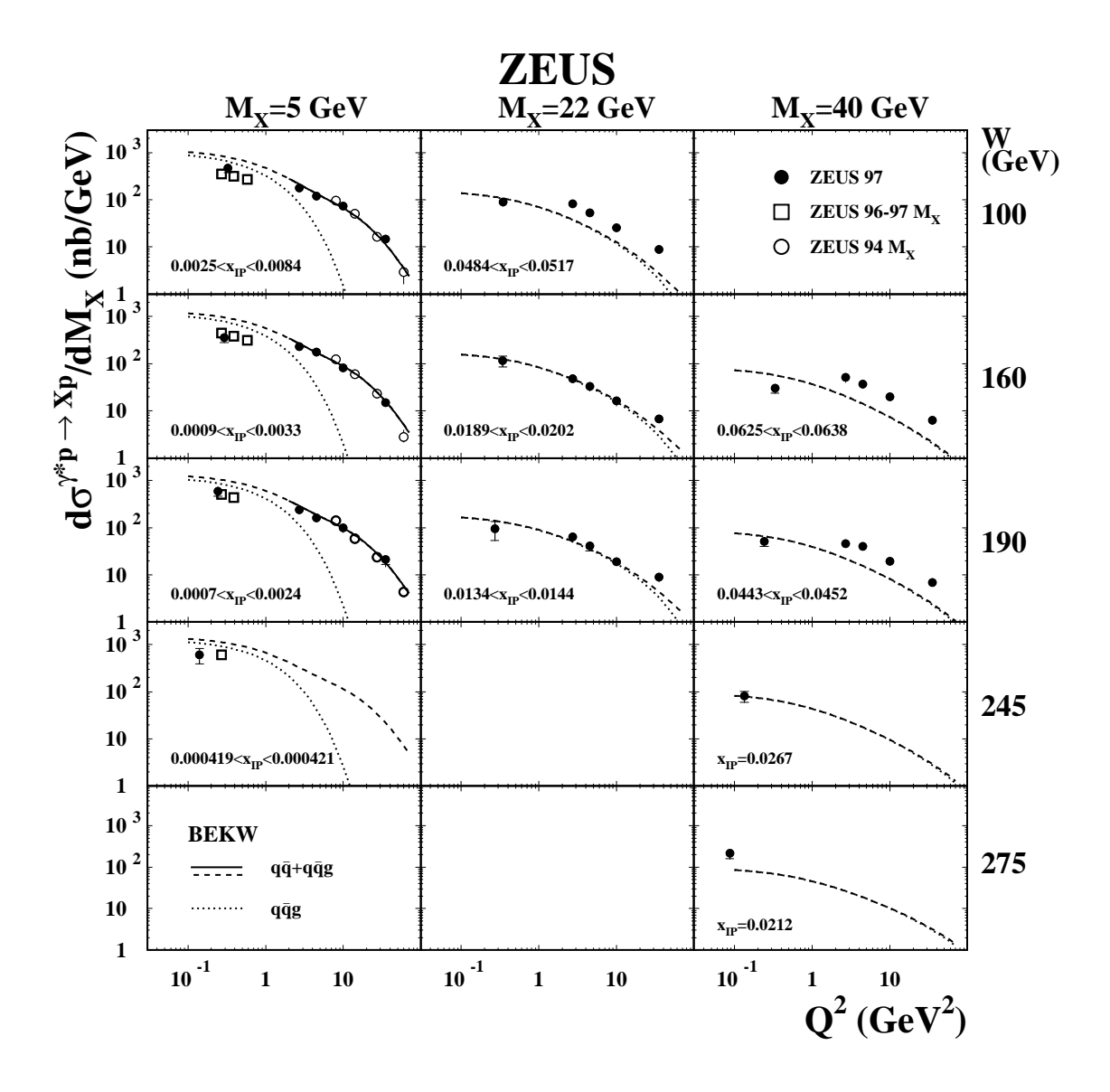


Figure 7: The cross-section $d\sigma^{\gamma^*p\to Xp}/dM_X$ as a function of Q^2 at different M_X and W values. The inner error bars show the statistical uncertainties and the full bars indicate the statistical and the systematic uncertainties added in quadrature; in several bins the size of the bars is smaller than that of the symbol used for the points. The overall normalisation uncertainty of $^{+12}_{-10}\%$ is not shown. The symbols labelled ZEUS 97 indicate the present results. Earlier ZEUS results are also shown: ZEUS 96-97 M_X [7], ZEUS 94 M_X [9]. The solid lines are the result of the BEKW fit to the present high- Q^2 data, described in Section 10.7.1; the dashed lines indicate the extrapolation outside the fit region. The dotted lines indicate the $q\bar{q}g$ contribution. The $x_{\mathbb{P}}$ ranges given refer to the coverage of the data.

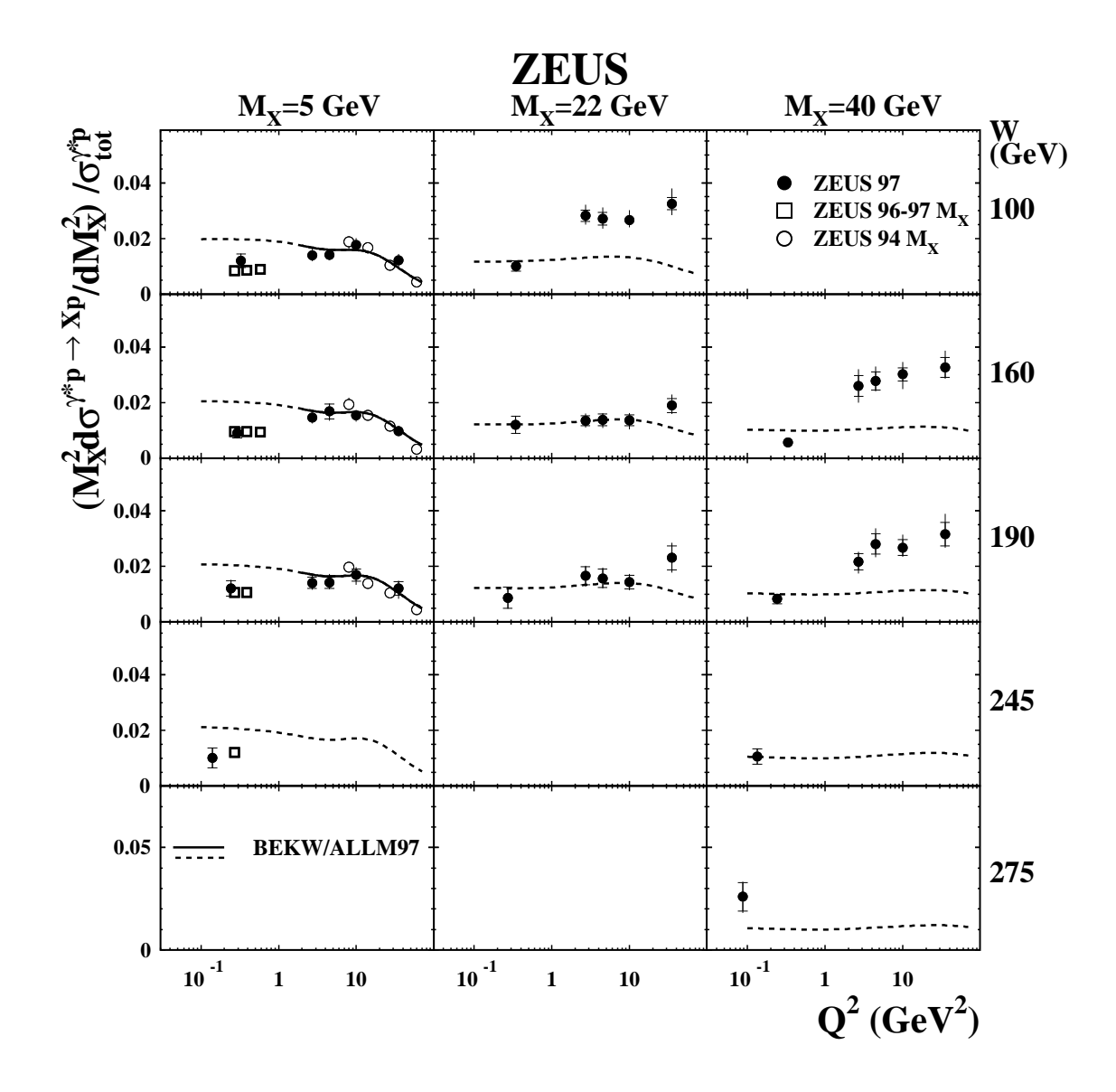


Figure 8: The ratio of $M_X^2 d\sigma^{\gamma^* p \to Xp}/dM_X^2$ to the total virtual photon proton cross section as a function of Q^2 at different M_X and W values. The inner error bars show the statistical uncertainties and the full bars indicate the statistical and the systematic uncertainties added in quadrature. The overall normalisation uncertainty of $^{+12}_{-10}\%$ is not shown. Earlier ZEUS results are also shown: ZEUS 96-97 M_X [7], ZEUS 94 M_X [9]. The solid lines are the result of the BEKW fit divided by the ALLM97 parameterisation, as described in Section 10.7.1. The dashed lines indicate the extrapolation outside the fit region.

ZEUS

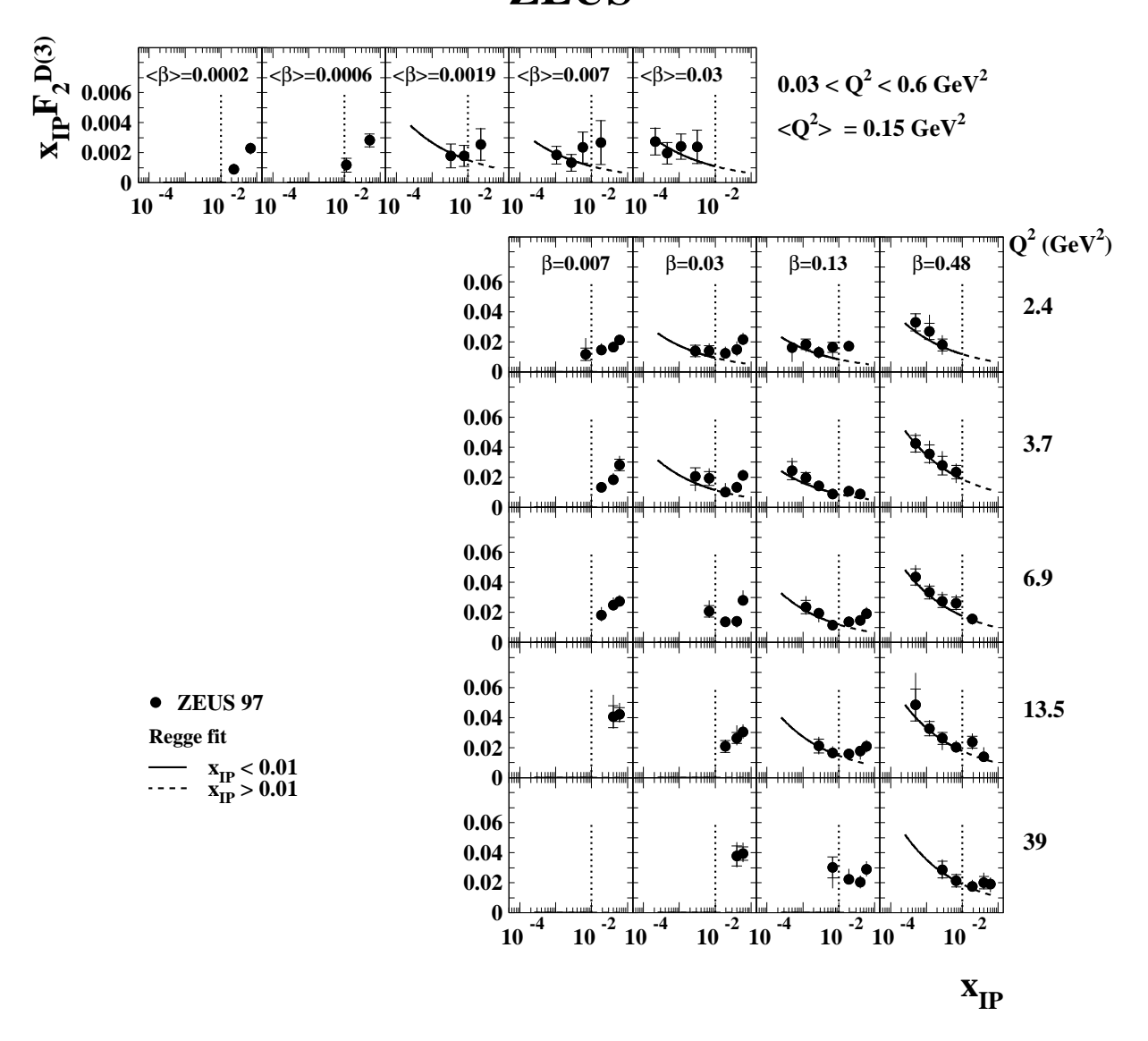


Figure 9: The diffractive structure function multiplied by $x_{\mathbb{P}}$, $x_{\mathbb{P}}F_2^{D(3)}(\beta, Q^2, x_{\mathbb{P}})$, as a function of $x_{\mathbb{P}}$, for different values of β and Q^2 . The inner error bars show the statistical uncertainties and the full bars indicate the statistical and the systematic uncertainties added in quadrature. In some bins the size of the bars is smaller than that of the symbol used for the points. The overall normalisation uncertainty of $^{+12}_{-10}\%$ is not shown. The vertical dotted lines indicate $x_{\mathbb{P}} = 0.01$. For the low- Q^2 points, the average value of Q^2 in each β - $x_{\mathbb{P}}$ bin varies between 0.10 and 0.22 GeV² (see Table 5). The solid lines show the result of the Regge fit described in Section 10.6. The dashed curves are the extension of the fit for $x_{\mathbb{P}} > 0.01$.

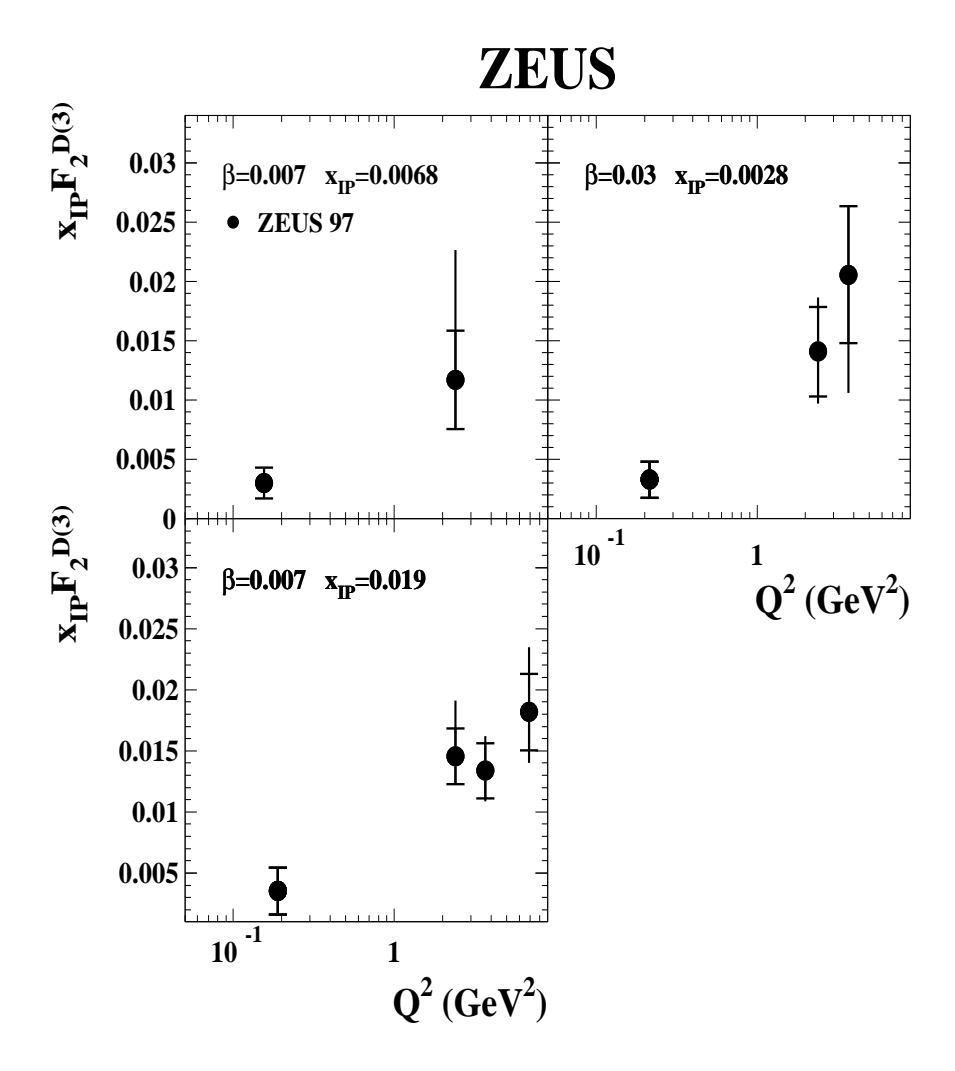


Figure 10: The diffractive structure function multiplied by $x_{\mathbb{IP}}$, $x_{\mathbb{IP}}F_2^{D(3)}(\beta, Q^2, x_{\mathbb{IP}})$, as a function of Q^2 , for the low- and high- Q^2 data, in the β - $x_{\mathbb{IP}}$ region in which the two data-sets overlap. The inner error bars show the statistical uncertainties and the full bars indicate the statistical and the systematic uncertainties added in quadrature. The overall normalisation uncertainty of $^{+12}_{-10}\%$ is not shown. The data shown here are those presented in Table 5 rebinned in x_L slightly for plotting purposes.

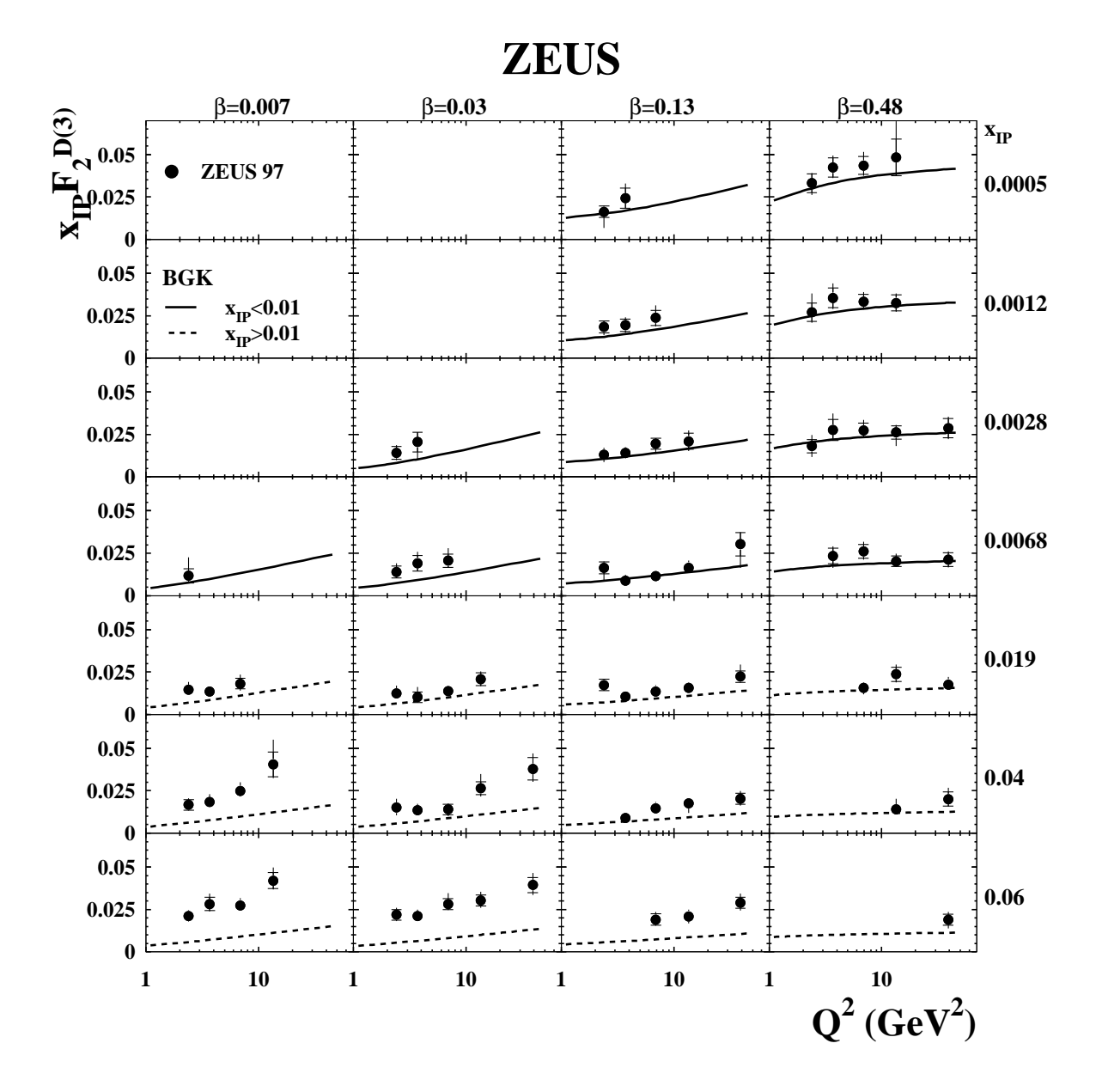


Figure 11: The diffractive structure function multiplied by $x_{\mathbb{P}}$, $x_{\mathbb{P}}F_2^{D(3)}(\beta, Q^2, x_{\mathbb{P}})$, as a function of Q^2 , for different values of $x_{\mathbb{P}}$ and β . The inner error bars show the statistical uncertainties and the full bars indicate the statistical and the systematic uncertainties added in quadrature. The overall normalisation uncertainty of $^{+12}_{-10}\%$ is not shown. The solid lines are the prediction of the saturation model of Bartels et al. [51] (BGK) discussed in Section 10.7.2; the dashed lines indicate the extrapolation of the model beyond $x_{\mathbb{P}} = 0.01$.

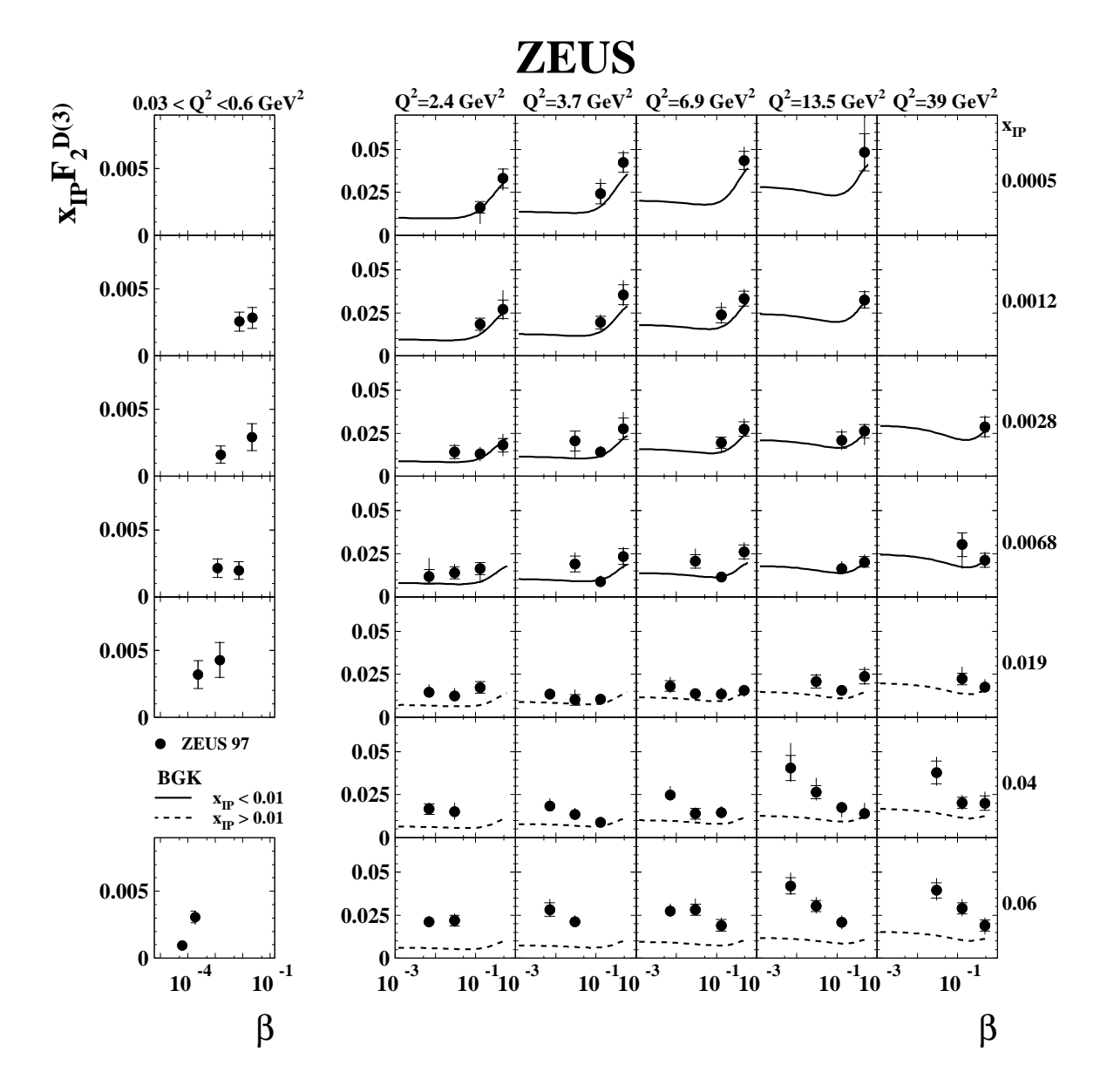


Figure 12: The diffractive structure function multiplied by $x_{\mathbb{IP}}$, $x_{\mathbb{IP}}F_2^{D(3)}(\beta,Q^2,x_{\mathbb{IP}})$, as a function of β , for different values of $x_{\mathbb{IP}}$ and Q^2 . The inner error bars show the statistical uncertainties and the full bars indicate the statistical and the systematic uncertainties added in quadrature. The overall normalisation uncertainty of $^{+12}_{-10}\%$ is not shown. The low- Q^2 data in the bin labelled $x_{\mathbb{IP}}=0.06$ have $x_{\mathbb{IP}}=0.067$ and $x_{\mathbb{IP}}=0.066$, respectively (see Table 6). The solid lines are the prediction of the saturation model of Bartels et al. [51] (BGK) discussed in Section 10.7.2; the dashed lines indicate the extrapolation of the model beyond $x_{\mathbb{IP}}=0.01$.

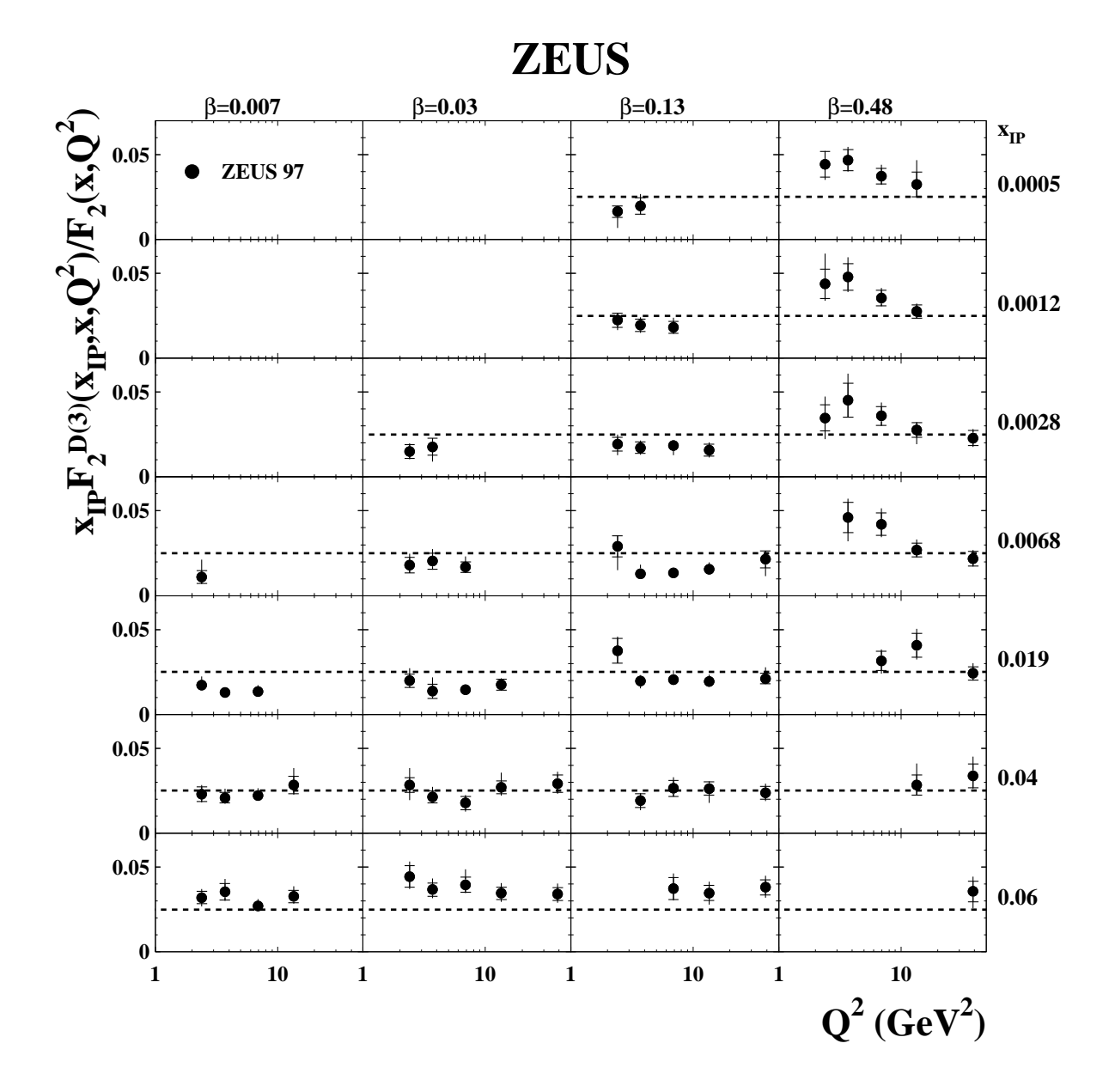


Figure 13: The ratio of the diffractive to the inclusive structure functions, $x_{\mathbb{IP}}F_2^{D(3)}(x_{\mathbb{IP}},x,Q^2)/F_2(x,Q^2)$, as a function of Q^2 at different values of $x_{\mathbb{IP}}$ and x. The values of $F_2(x,Q^2)$ were obtained from the ALLM97 parameterisation. The inner error bars show the statistical uncertainties and the full bars indicate the statistical and the systematic uncertainties added in quadrature. The overall normalisation uncertainty of $^{+12}_{-10}\%$ is not shown. The horizontal lines indicate the average value of the ratio and are only meant to guide the eye.

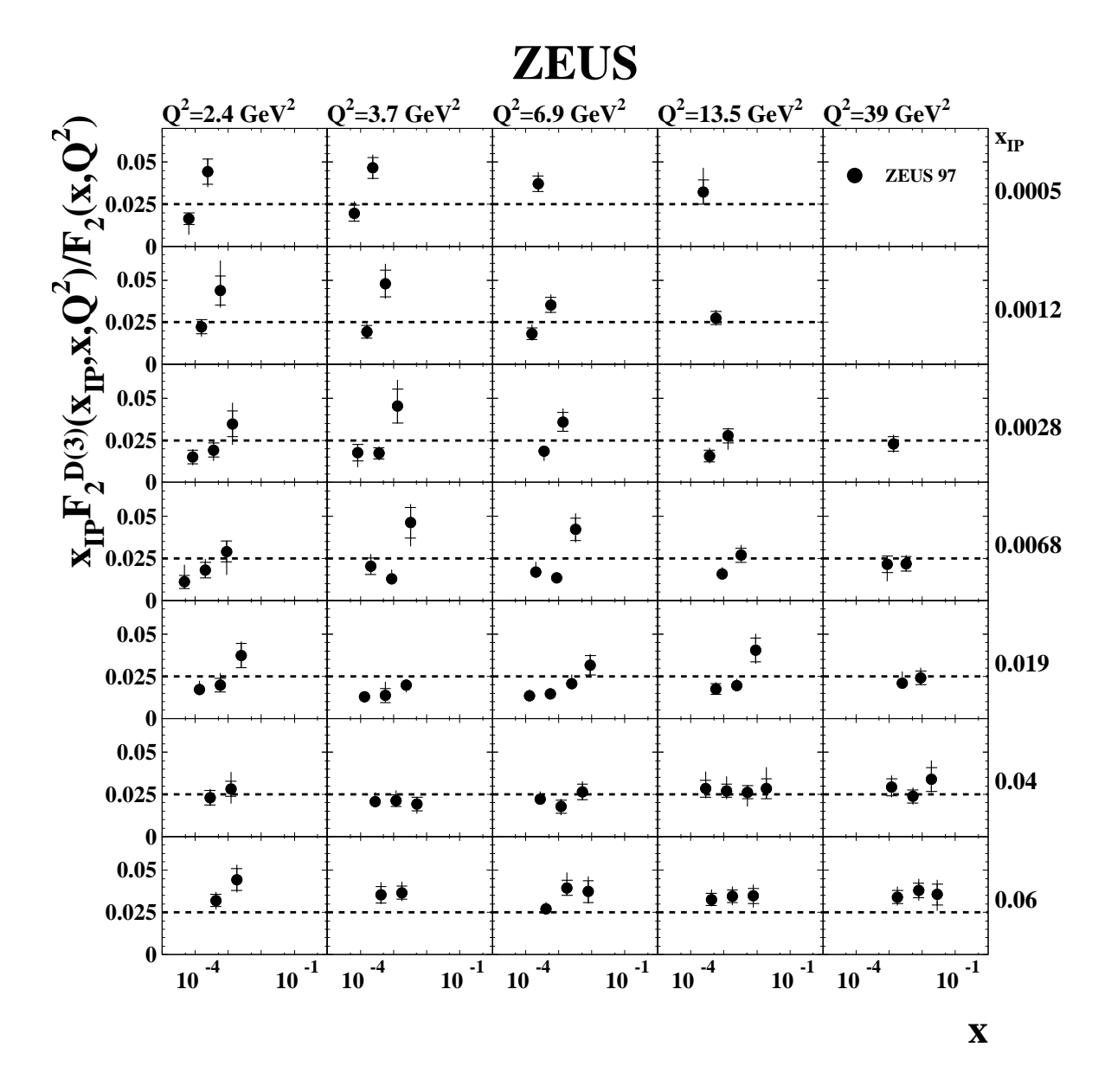


Figure 14: The ratio of the diffractive to the inclusive structure functions, $x_{\mathbb{P}}F_2^{D(3)}(x_{\mathbb{P}},x,Q^2)/F_2(x,Q^2)$, as a function of x at different values of $x_{\mathbb{P}}$ and Q^2 . The values of $F_2(x,Q^2)$ were obtained from the ALLM97 parameterisation. The inner error bars show the statistical uncertainties and the full bars indicate the statistical and the systematic uncertainties added in quadrature. The overall normalisation uncertainty of $^{+12}_{-10}\%$ is not shown. The horizontal lines indicate the average value of the ratio and are only meant to guide the eye.

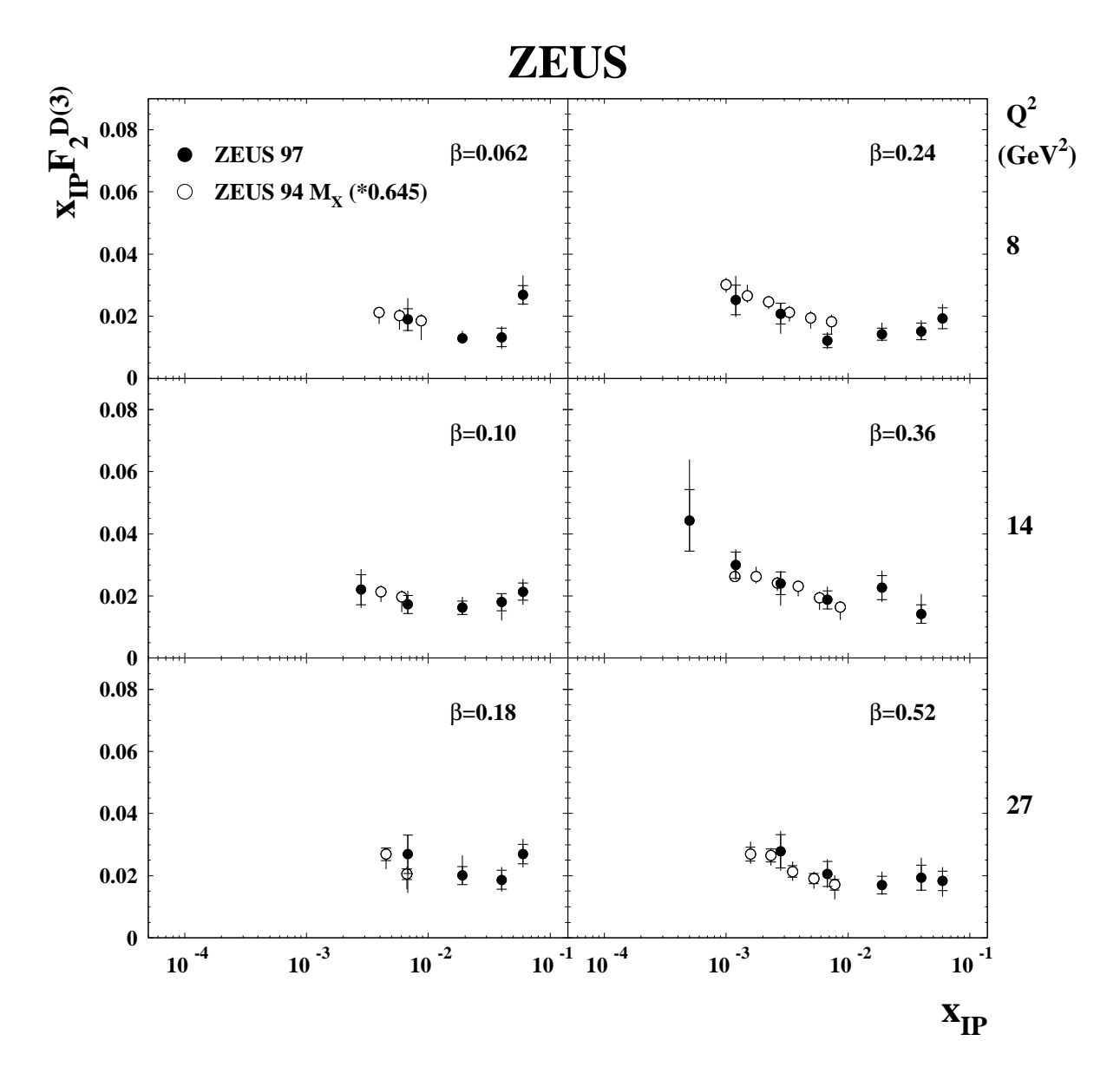


Figure 15: The diffractive structure function multiplied by $x_{\mathbb{P}}$, $x_{\mathbb{P}}F_2^{D(3)}(\beta,Q^2,x_{\mathbb{P}})$ as a function of $x_{\mathbb{P}}$, for different values of β and Q^2 for the LPS and M_X -method [9] analyses; the latter points are rescaled by $1/R_{M_X}=0.645$, as discussed in the text. The inner error bars show the statistical uncertainties and the full bars indicate the statistical and the systematic uncertainties added in quadrature. The overall normalisation uncertainties of $^{+12}_{-10}\%$ (LPS data) and 2% (M_X -method data) are not shown.

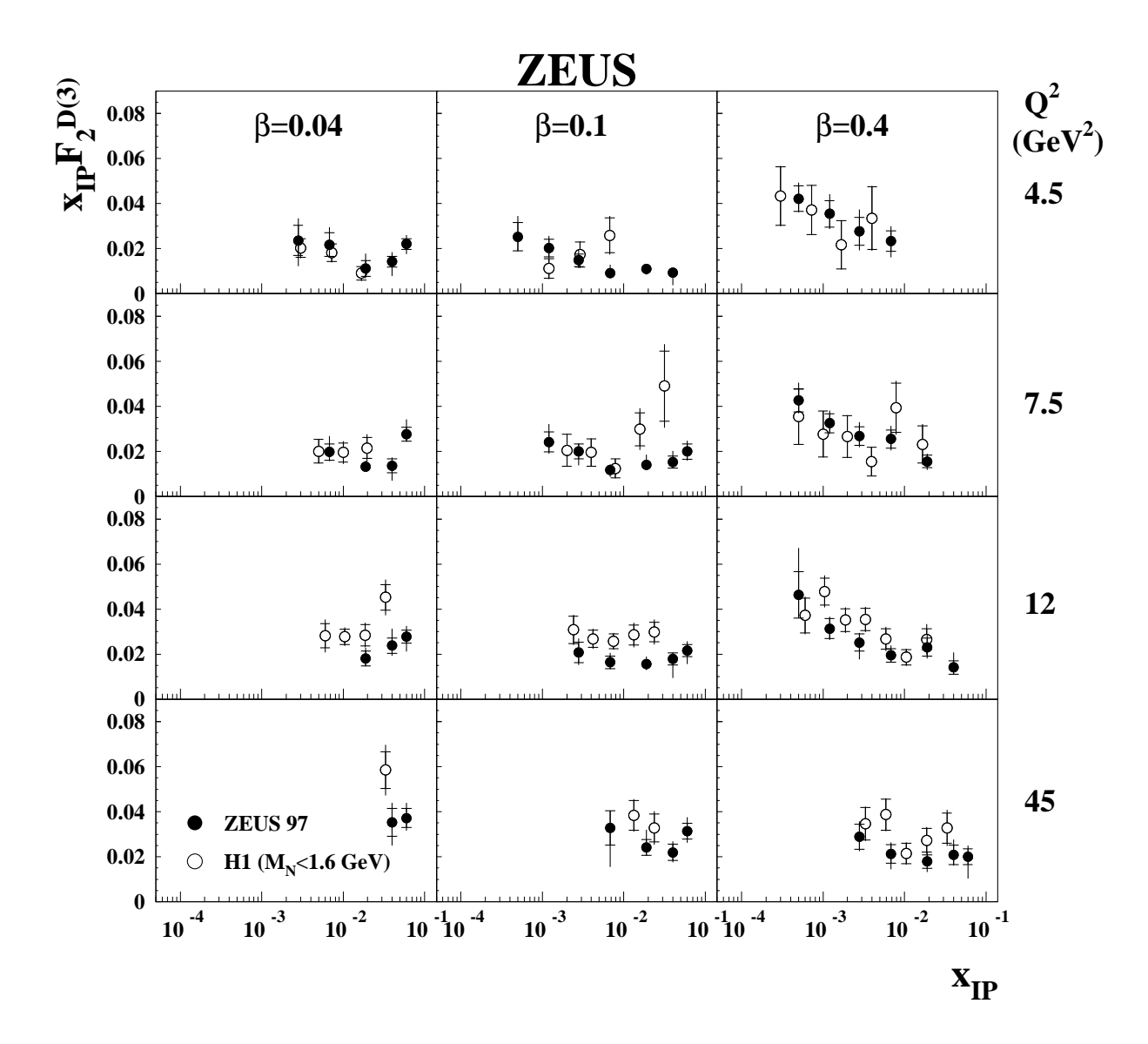


Figure 16: The diffractive structure function multiplied by $x_{\mathbb{IP}}$, $x_{\mathbb{IP}}F_2^{D(3)}(\beta,Q^2,x_{\mathbb{IP}})$ as a function of $x_{\mathbb{IP}}$, for different values of β and Q^2 for the LPS and the H1 data [14]. The inner error bars show the statistical uncertainties and the full bars are the statistical and the systematic uncertainties added in quadrature. The overall normalisation uncertainties of $^{+12}_{-10}\%$ (LPS data), $\pm 6\%$ (H1 data, $Q^2 < 9 \text{ GeV}^2$) and $\pm 4.8\%$ (H1 data, $Q^2 > 9 \text{ GeV}^2$) are not shown.

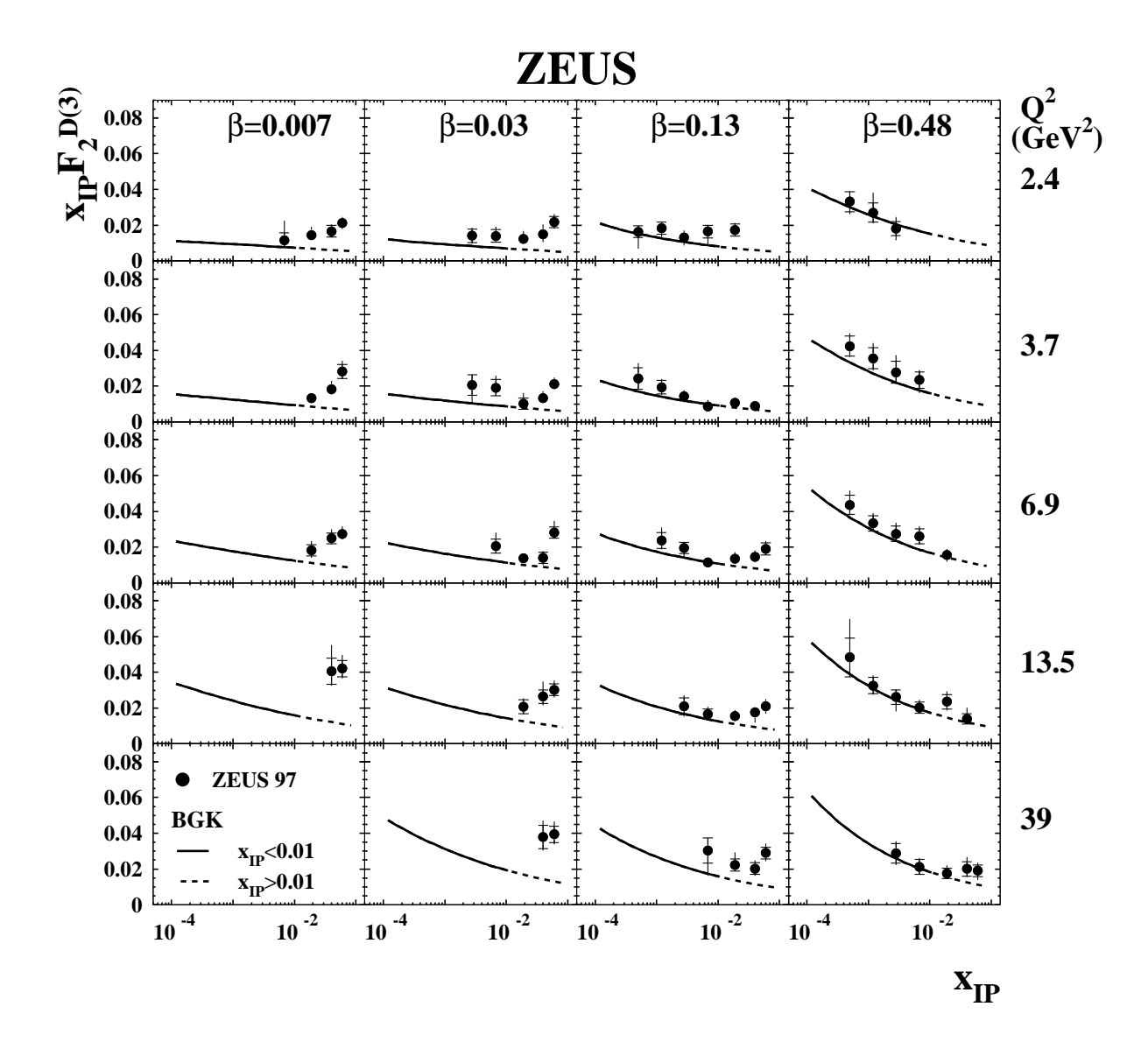


Figure 17: The diffractive structure function multiplied by $x_{\mathbb{P}}$, $x_{\mathbb{P}}F_2^{D(3)}(\beta, Q^2, x_{\mathbb{P}})$, as a function of $x_{\mathbb{P}}$, for different values of β and Q^2 . The inner error bars show the statistical uncertainties and the full bars indicate the statistical and the systematic uncertainties added in quadrature. The overall normalisation uncertainty of $^{+12}_{-10}\%$ is not shown. The solid lines are the prediction of the saturation model of Bartels et al. [51] (BGK) and are discussed in Section 10.7.2. The dashed curves are the extrapolation of the model prediction for $x_{\mathbb{P}} > 0.01$.

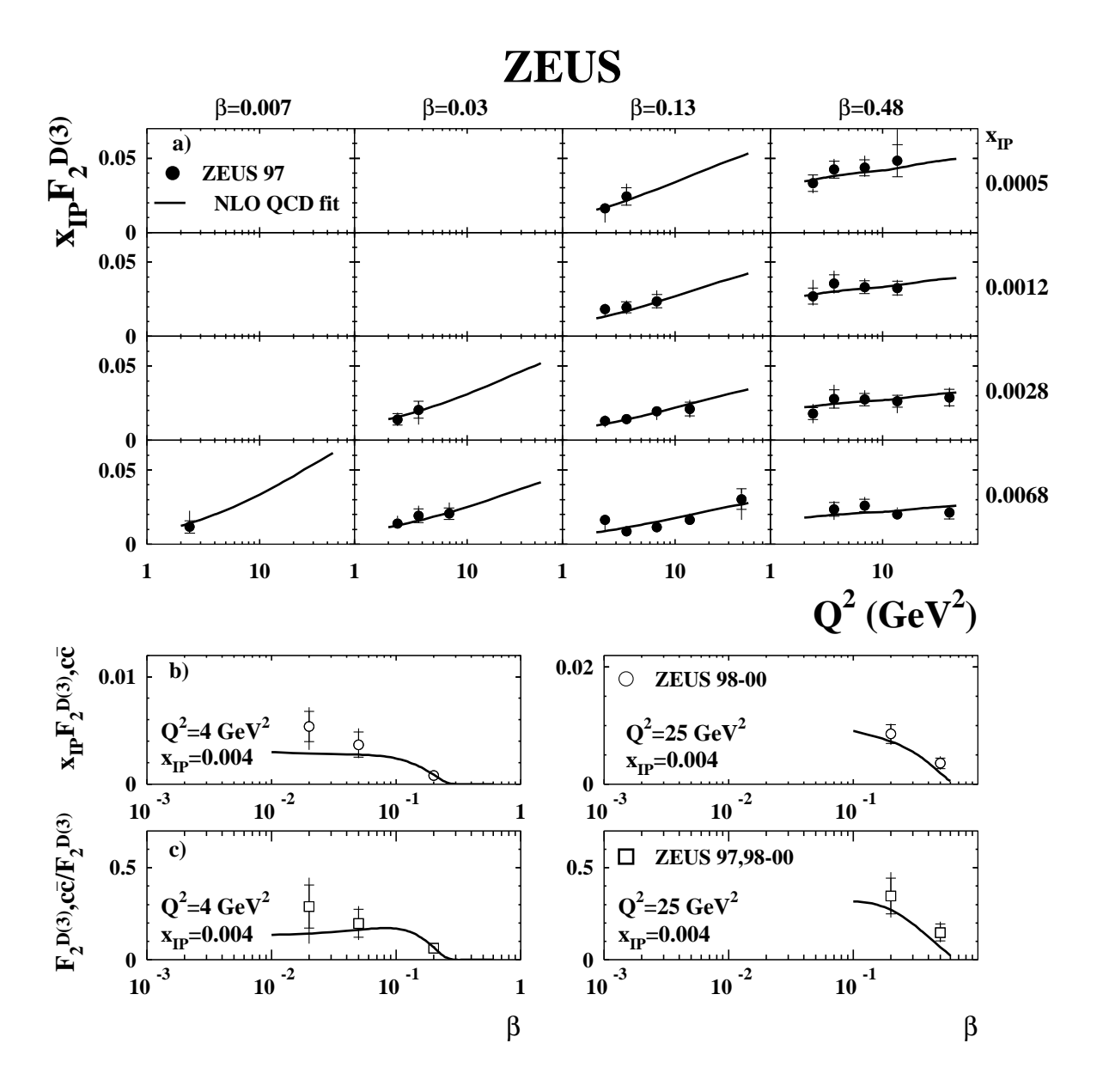


Figure 18: (a) The diffractive structure function multiplied by $x_{\mathbb{IP}}$, $x_{\mathbb{IP}}F_2^{D(3)}(\beta,Q^2,x_{\mathbb{IP}})$, as a function of Q^2 , for different values of $x_{\mathbb{IP}}$ and β . The inner error bars show the statistical uncertainties and the full bars are the statistical and the systematic uncertainties added in quadrature. The overall normalisation uncertainty of $^{+12}_{-10}\%$ is not shown. (b) The measured charm contribution to the diffractive structure function multiplied by $x_{\mathbb{IP}}$, $x_{\mathbb{IP}}F_2^{D(3),c\bar{c}}(\beta,Q^2,x_{\mathbb{IP}})$, as a function of β , for different values of Q^2 and $x_{\mathbb{IP}}=0.004$ [56]. (c) The ratio of $F_2^{D(3),c\bar{c}}$ [56] and the present $F_2^{D(3)}$ measurement as a function of β . The solid lines are the result of QCD NLO fit described in the text.